ACS OMEGA

http://pubs.acs.org/journal/acsodf

Article

Catalytic Decomposition of Residual Ozone over Cactus-like MnO_2 Nanosphere: Synergistic Mechanism and SO_2/H_2O Interference

Hairong Tang, Zhihua Wang,* Jiaming Shao, Fawei Lin, Peixi Liu, Yong He, and Yanqun Zhu

Cite This: *ACS Omega* 2022, 7, 9818−9833

Read Online

ACCESS | Metrics & More | Article Recommendations | Supporting Information

ABSTRACT: Ground-level ozone is an irritant and is harmful to human respiratory and nervous systems. Thus, four manganese oxides with different crystals were hydrothermally synthesized to decompose residual ozone (deO_3) in an ozone synergistic−oxidation system. Among them, a cactus-like MnO_2-IV nanosphere exhibited the highest deO_3 activity, with excellent tolerance to water vapor and SO_2/H_2O, which could maintain >88% deO_3 efficiency in the high-humidity and sulfur-containing conditions. It benefits from the unique morphology, high specific surface area, superior redox properties, oxygen chemisorption capabilities, abundant surface-active hydroxyl species, and low valence Mn species. More importantly, the detailed interference mechanism of $O_2/O_3/H_2O/SO_2$ molecules on MnO_2-IV was revealed utilizing in situ diffused reflectance infrared Fourier transform spectroscopy and X-ray photoelectron spectroscopy. H_2O generally caused recoverable deactivation, but that caused by SO_2 was irreversible. The synergistic effect of SO_2/H_2O promoted the formation of an unstable sulfate species, thereby deepening the deactivation but inhibiting the irreversible poisoning. Finally, nine specific steps to decompose ozone via surface-active hydroxyl/intermediates were established.

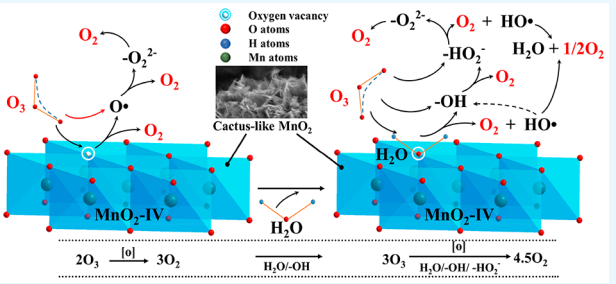

1. INTRODUCTION

Ozone has strong oxidizing properties and is one of the strongest oxidants in nature. Excess ground-level ozone is an irritant and is harmful to human respiratory and nervous systems,[1] which can cause serious respiratory symptoms like coughing, chest tightness, and tachypnea.[2,3] Moreover, breathing ambient air containing ozone can induce asthma symptoms.[4,5] Commonly, ground-level ozone can be generated naturally via photochemical reactions under conditions of high temperature, sufficient sunshine, and dry air. Nowadays, anthropogenic ground-level ozone, derived from the nitrogen oxides (NO_x) and volatile organic compounds (VOCs), has been listed as one of the main air pollutants.[6,7] Therefore, a lot of work has been devoted to controlling the emission of air pollutant precursors. Furthermore, the emissions and unorganized diffusion issues of indoor residual ozone are also important, such as wastewater treatment,[8] disinfection,[9] air purifiers,[10] laser printers, and so on. For these occasions where ozone is actively generated and released, more work has been devoted to controlling (indoor) ozone emission under simple gas components. However, there is still a lack of research on complex industrial conditions.

Recently, ozone synergistic−oxidation technology has been rapidly applied to industries for flue gas treatment.[11−14] These medium-sized boilers/furnaces in biomass power plants,[11] thermal power plants, and industries such as rubber,[12] glass,[13] and waste incineration[14] are limited by space, flue gas conditions, and capital, resulting in unavailable application of traditional selective noncatalytic reduction (SNCR) technology and selective catalytic reduction (SCR) technology for NO_x abatement.[15] In contrast, ozone can preferentially convert insoluble NO into highly soluble NO_2/N_2O_5 at a low temperature (80−140 °C),[16,17] whereas SO_2 cannot be oxidized by ozone under these conditions. Further, the insoluble mercury and VOCs can also be oxidized into soluble Hg^{2+} and environmentally friendly CO_2 and H_2O by O_3, respectively.[18] Subsequently, the oxidized soluble NO_2, N_2O_5, Hg^{2+}, and CO_2 can be absorbed together with SO_2 in a wet scrubber.[19] It is advantageous that the original wet flue gas desulfurization (WFGD) system can undertake the absorption functions and achieve a simultaneous multipollutant removal function. However, due to the load/fuel fluctuations in actual engineering applications, residual ozone can be detected in the exhaust gas especially when excess ozone is injected to achieve a higher denitration efficiency. Sometimes residual ozone even reaches up to ∼22 ppm under the molar ratio of O_3/NO around 2.9,[11] which exceeds the standards of 50 ppb (suggested by World Health Organization) and 0.16 mg/m^3

Received: January 7, 2022
Accepted: February 28, 2022
Published: March 8, 2022

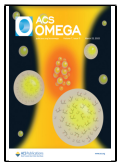

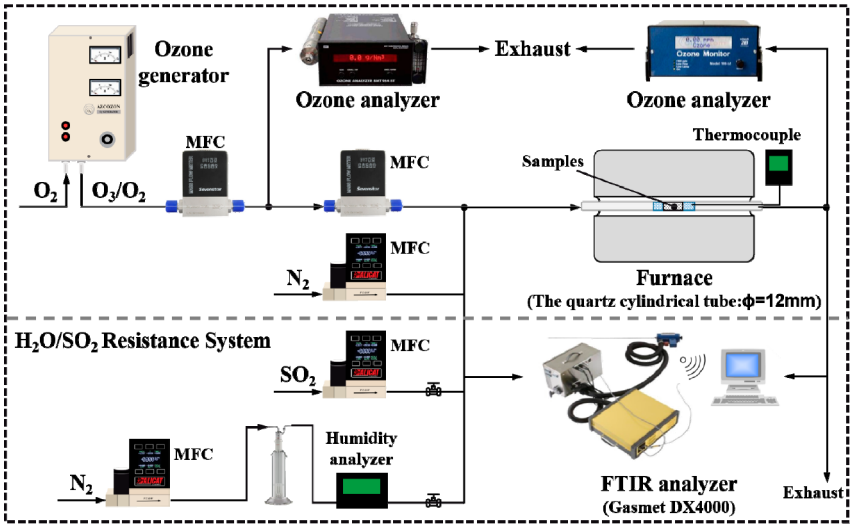

Figure 1. Schematic diagram of the O_3 decomposition experimental setup.

(~0.7 ppm, suggested by Indoor Air Quality Standard (GB/T 18883-2002, China)).[20−22] The residual ozone has already received public attention and has hindered the applications of ozonation technology. Therefore, there is an urgent need to develop an effective method to eliminate the residual ozone, especially one that can adapt to the complex flue gas conditions.

So far, the reported technologies to eliminate ozone include activated carbon adsorption,[23] liquid absorption,[24] thermal decomposition,[25] and direct catalytic decomposition. Among them, the direct catalytic decomposition method, benefiting from its stability, safety, and economy, is considered as the most promising way to achieve nonhazardous disposal of ozone. In terms of non-noble catalysts, manganese-based catalysts generally exhibit excellent low-temperature activity and promote the decomposition of ozone (deO_3).[26,27] Therefore, considerable research has been devoted to revealing the deO_3 mechanism of Mn-based catalysts. As shown in eqs 1−3, the widely accepted mechanism consists of the dissociative adsorption of O_3 and the desorption of adsorbed intermediates (the symbol * represents active sites).[28−30] Research shows that manganese oxides can form various crystals with different tunnel structures through MnO_6 octahedra units, which provide abundant active sites and oxygen vacancies.[27,31] Herein, surface oxygen vacancies can significantly improve the adsorption and decomposition of O_3 molecules.[30] Furthermore, the surface defections and low valence Mn^{2+}/Mn^{3+} species in the structure also play key roles in the ozone decomposition process.[32] In addition to pure MnO_x, the deO_3 behaviors of supported MnO_x catalysts are closely related to the characteristics of support and the loading situation of Mn species. For instance, the deO_3 activity of MnO_x/ZSM-5 zeolite is related to the surface acidic sites and hydrophobicity of the ZSM-5 support.[20,33] Zhu et al. obtained α-MnO_2 nanofibers with a high concentration of surface oxygen vacancies by vacuum deoxidation, which increased their ozone removal rate from 32.6 to 95% in dry gas flow.[30] Moreover, the specific intermediate and binding method of O_3 molecules adsorbed on the Mn-based samples is also a hot research topic, which has not yet been further explored. For example, $Mn(OH)_4(O_2)^+$ species on MnO_x/Al_2O_3 are considered to be the possible compound for the adsorbed oxygen species.[28] Given that the complex compositions in flue gas and water vapor can cause catalyst deactivation, it is an important factor for the deO_3 applications. For example, the ozone removal rate of α-MnO_2 nanofibers at 12 h decreased from 97 to 48%, whereas the relative humidity (RH) increased from <5 to 30%.[30] Doping and modifing (K,[34] Na,[35] Fe,[21] Ni,[36] and Ce,[37] etc.) could adjust the average valence of Mn and promote the oxygen vacancies, thus obtaining a better deO_3 performance and water vapor resistance capability. $MnFe_{0.5}O_x$ catalyst modified by Fe atoms has more abundant surface Mn^{3+} (Mn^{2+}) species and can maintain over 85% ozone conversion under >90% RH.[21] Nevertheless, most of the above-mentioned work was aimed at a simple application condition. The interference mechanism of water vapor on ozone decomposition is generally unclear, especially under the complex flue gas containing multiple components.

$$O_3(g) + * \rightarrow O^* + O_2(g) \quad (1)$$

$$O_3(g) + O^* \rightarrow O_2(g) + O_2^* \quad (2)$$

$$O_2^* \rightarrow O_2(g) + * \quad (3)$$

In summary, the existing research on O_3 decomposition has made relatively good progress in catalyst synthesis and decomposition mechanism. However, detailed literature on high humidity and low sulfur conditions is rare, resulting in a few useful works when dealing with residual O_3 in the ozone synergistic−oxidation system. In particular, under sulfur-containing and humidity conditions, the specific changes of the intermediate product and the deactivation mechanism on the catalyst surface are still unclear. To the best of our knowledge, there is no report for ozone elimination closely integrated with the actual flue gas conditions of the ozone synergistic−oxidation system.

Hence, this work was devoted to revealing the decomposition behavior of O_3 molecules on hydrothermally synthesized manganese oxides, especially with the interference of water vapor and SO_2. Notably, the detailed $O_3/O_2/H_2O/SO_2$ adsorption behaviors on cactus-like MnO_2 were revealed utilizing in situ diffused reflectance infrared Fourier transform spectroscopy (DRIFTS) and X-ray photoelectron spectroscopy (XPS). More importantly, a novel mechanism in which ozone molecules are decomposed via the surface-active hydroxyl

https://doi.org/10.1021/acsomega.2c00120
ACS Omega 2022, 7, 9818−9833

species was proposed. This work provides deeper insight into residual ozone decomposition and promotes the industrial applications of affordable Mn-based catalysts in the ozone synergistic−oxidation system.

2. EXPERIMENTAL METHODOLOGY

2.1. Preparation of Catalysts. Four manganese oxides with different crystalline structures (abbreviated as MnO_2-I, MnO_2-II, MnO_2-III, and MnO_2-IV) were synthesized by a uniform hydrothermal method. In the synthesis of MnO_2-I, 16 mmol $KMnO_4$ (Sinopharm, China) and 6 mmol $MnSO_4{\cdot}H_2O$ (Sinopharm, China) were dissolved in 160 mL of deionized water under ultrasonic stirring for 20 min, and the solution was kept at 140 °C for 12 h in a 200 mL Teflon-lined autoclave. The precipitation was further dried at 110 °C for 12 h after thorough centrifugation and washing, and then the obtained powder was annealed at 300 °C for 3 h in air. The syntheses of MnO_2-II, MnO_2-III, and MnO_2-IV were similar to that of MnO_2-I except for the differences of precursors and hydrothermal conditions. Specifically, MnO_2-II was synthesized with $(NH_4)_2S_2O_8$ (Sinopharm, 10 mmol) and $MnSO_4{\cdot}H_2O$ (10 mmol). For MnO_2-III, the solution with $(NH_4)_2S_2O_8$ (16 mmol) and $MnSO_4{\cdot}H_2O$ (16 mmol) was hydrothermally reacted at 90 °C for 24 h. Further, MnO_2-IV was synthesized via the hydrothermal reaction of $KMnO_4$ (36 mmol) and $MnSO_4{\cdot}H_2O$ (6 mmol) at 240 °C for 24 h. All of the reagents were of analytical grade, and the catalysts were screened with 40−60 mesh before the activity tests.

2.2. Activity Tests. The O_3 decomposition activity and SO_2/H_2O resistance tests of the synthesized manganese oxides were evaluated in a fixed-bed furnace, and the schematic diagram is shown in Figure. 1. The experimental setup consisted of a gas-feeding system, an ozone generation−detection system, an electric heated reaction furnace, and a Fourier transform infrared (FTIR) analyzer. Source gas was supplied from cylinder bottles (Hangzhou Jingong Special Gas Co., Ltd., 99.999% for O_2, 99.999% for N_2, 1000 ppm/balance N_2 for SO_2) and controlled by mass flow controllers (MFCs, O_3/O_2, Beijing Sevenstar Electronics Co., Ltd.; N_2, SO_2, Alicat Scientific, Inc.). Ozone was generated by a dielectric barrier discharge (DBD) reactor (VMUS-1S, AZCO Industries., Ltd.) and divided into two parts. The initial O_3 concentration was monitored by a high concentration ozone analyzer (BMT-964B, OSTI, Inc., range: 0−20 g/Nm^3, resolution: 0.1 g/Nm^3), and then one O_3/O_2 stream was mixed with N_2 according to the calculated molar ratio. The residual O_3 after decomposition was measured by a dual beam ozone monitor (model 205, 2B Technologies, Inc., 0−250 ppm, resolution 0.1 ppb). The reaction furnace was equipped with a K-type thermocouple inserted to monitor the reaction temperature.

In each test, 0.15 g of MnO_2 was mixed with quartz sand (SiO_2, Sinopharm, 40−60 mesh) and placed in a quartz cylindrical tube (inner diameter: 12 mm). The total flow rate was kept at approximately 1.5 L/min with the gas hour space velocity (GHSV) of ∼30000 h^{-1} (or ∼90000 h^{-1}), and the initial O_3 concentration in the mixed gas was ∼100 ppm. For facilitating comparison and multiple replicates, the activity data after a 300 min test were used to investigate their deO_3 performance, and the stability results (MnO_2-IV, 12 h) are shown in the Supporting Information (Figure S1). Subsequently, MnO_2-IV was selected to do further tolerance investigations because of its highest activity among four manganese oxides. The H_2O/SO_2 tolerance tests were performed based on the high-humidity gas conditions and "ultralow emission" standards (SO_2 < 35 mg/Nm^3) after the scrubber. Water vapor or 10 ppm (28.57 mg/Nm^3) SO_2 was introduced into the reactor after a 60 min stabilization at 80 °C to investigate the catalytic tolerance to water vapor and SO_2. Water vapor was carried via a nitrogen flow by the heating−bubbling method and measured by a humidity analyzer (TH21E, Anymetre, Inc.). The inlet and outlet concentrations of SO_2 were monitored with a Gasmet DX4000 FTIR analyzer. The O_3 decomposition efficiency was calculated by the following eq 4:

$$\eta_{O_3} = \frac{[O_3]_{inlet} - [O_3]_{outlet}}{[O_3]_{inlet}} \times 100\% \quad (4)$$

where η_{O_3} represents the ozone decomposition efficiency of the catalyst. $[O_3]_{inlet}$ and $[O_3]_{outlet}$ represent the initial and outlet ozone concentration in parts per million, respectively.

2.3. Catalyst Characterization. Powder X-ray diffraction (XRD) patterns were obtained on a Rigaku D/max 2550PC diffractometer using monochromatized Cu Kα radiation (λ = 1.5406 Å, step size = 0.5°, 4° min^{-1} from 10 to 80°). The surface area of catalyst was determined by the Brunauer−Emmett−Teller (BET) model from nitrogen adsorption−desorption isotherms (at 77 K, Gemini V2380 chemical adsorption analyzer). Moreover, the Barrett−Joyner−Halenda (BJH) method was used to calculate pore volume and average pore diameter. The micromorphology of the catalyst was detected on a Hitachi SU-70 field emission scanning electron microscope (FE-SEM). X-ray photoelectron spectra were recorded on a Thermo Scientific ESCALAB 250Xi analyzer using a standard Al Kα source (1486.6 eV), and all binding energies are referenced to the C 1s peak at 284.8 eV.

The hydrogen temperature-programmed reduction (H_2-TPR) and oxygen temperature-programmed desorption (O_2-TPD) measurements were conducted on a Micromeritics AutoChem II 2920 chemical adsorption analyzer with a thermal conductivity (TCD) detector. In the H_2-TPR test, ∼50 mg of catalyst was loaded in the U-type quartz tube to undergo the pretreatment. The sample was first purged at 200 °C for 1 h under 30 mL/min of He flow and then cooled naturally to 100 °C. After stabilization, the program was heated to 800 °C (10 °C/min) under 20 mL/min of 5 vol % H_2/Ar flow, and the signal intensity was recorded by the TCD detector. The hydrogen consumption was referenced to the data of standard copper oxide and further quantified. For O_2-TPD, ∼50 mg of catalyst was similarly pretreated and then cooled to 50 °C. In the subsequent adsorption, the catalyst was treated in a 50 mL/min of 2 vol % O_2/He flow for 1 h and further purged under 30 mL/min of He for 50 min to remove residual gas as well as physically adsorbed species. Furthermore, the program was heated to 900 °C (10 °C/min) under 50 mL/min of He flow, and the TPD data were collected by a Hiden QIC20 mass spectroscope.

FTIR spectra of samples before/after the reactions were collected on a Thermo Nicolet iS50 FTIR spectrometer. Further, in situ DRIFTS data were conducted on an iS50 spectrometer equipped with a reaction chamber (Praying Mantis) and detected by a mercury cadmium telluride (MCT/A) detector. For each test, the catalyst was purged by 100 mL/min of N_2 flow at 150 °C for 30 min and then cooled naturally to 80 °C. Subsequently, the in situ spectra were recorded at a

https://doi.org/10.1021/acsomega.2c00120
ACS Omega 2022, 7, 9818−9833

resolution of 4 cm^{-1} in a 600−4000 cm^{-1} range under specific simulated flue gas conditions ($O_2/O_3/SO_2/H_2O$).

3. RESULTS AND DISCUSSION

3.1. Crystal Structures, Morphologies, and Textural Properties. Powder XRD data were collected to confirm the crystal structures of four synthesized MnO_x, and their patterns are shown in Figure 2. Figure S2 represented the standard

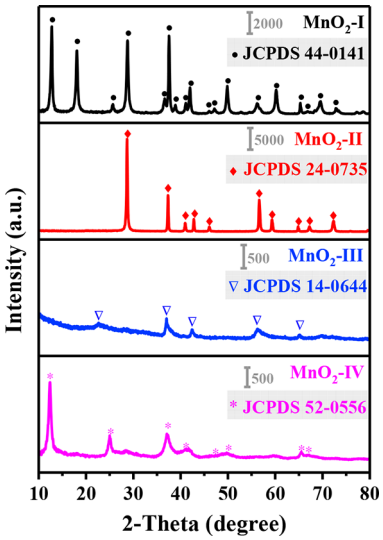

Figure 2. Powder XRD patterns of manganese oxides in the 2θ range of 10−80°.

XRD patterns of JCPDS 44-0141 (α-MnO_2),[38] JCPDS 24-0735 (pyrolusite, β-MnO_2),[39] JCPDS 14-0644 (nsutite, γ-MnO_2),[40] and JCPDS 52-0556 (birnessite-type potassium MnO_2, δ-MnO_2).[41,42] The diffraction pattern for the MnO_2-I sample exhibits typical characteristic peaks at 12.8, 18.1, 28.8, 37.5, 42.0, 49.9, 60.3, and 69.7°, corresponding to (110), (200), (310), (211), (301), (411), (521), and (541) planes of α-MnO_2, respectively. The MnO_2-II sample exhibits sharp peaks at 28.7, 37.3, 42.8, 56.7, 59.4, and 72.3° corresponding to (110), (101), (111), (211), (220), and (301) planes of β-MnO_2, respectively. Both MnO_2-I and MnO_2-II had sharp and intense diffraction peaks as well as no impurity peaks, indicating their highly crystalline nature and high purity.[43] Nevertheless, the diffraction patterns for MnO_2-III and MnO_2-IV were much weaker. The wide diffraction peaks with low intensities observed in MnO_2-III at 22.4, 37.1, 42.6, 56.1, and 65.6° were ascribed to (120), (131), (300), (160), and (421) planes of γ-MnO_2, indicating the poor crystallinity of γ-MnO_2 in MnO_2-III.[44] Additionally, the broad peaks with a slight shift at 12.4, 25.0, 37.1, 42.1, ∼49.7, and ∼65.5° observed over MnO_2-IV were partially assigned to (003), (006), (012), (015), (018), and (110) planes of δ-MnO_2, respectively. This indicated that there are weak crystallization and slight lattice defects associated with δ-MnO_2 in the MnO_2-IV phase. Further, the relatively intense diffraction peak at 12.4° ((003) plane) suggested that more MnO_6 octahedral units had extended growth along the plane, which possibly formed the local layered structures under the stabilization of plentiful K^+ or H_2O molecules as the template.[45] The XRD results confirmed that four high-purity manganese oxides with different crystals were successfully synthesized.

Scanning electron microscopy (SEM) measurements were collected to further distinguish morphologies and surface structures of the synthesized MnO_2. As shown in Figure 3a1,a2, SEM images showed that particles of MnO_2-I adopted a slender and regular rod-like morphology with diameters of 50−100 nm and lengths of 1−6 μm that tended to be randomly distributed and clustered in loose clusters. Moreover, SEM images (Figure 3b1,b2) presented that MnO_2-II mainly consisted of nanowires that were shorter but thicker than those of MnO_2-I, as well as a few flat-regular flakes with diameters of 150−400 nm. These morphologies coincided with the good crystallinity in their XRD results (Figure 2). Different from the former two with the randomly distributed nanorods/nanowires, SEM images of both MnO_2-III and MnO_2-IV exhibited some agglomerated particles. As shown in Figure 3c1,c2, SEM images of MnO_2-III catalysts presented some rough nanospheres with diameters of 3.5−10.0 μm, and each nanosphere was composed of closely packed nanowires as well as prolate agglomerated nanoflakes, confirming its weak crystallization in the XRD pattern. Further, Figure 3d1,d2 presents that MnO_2-IV consisted of cactus-like nanospheres, and the diameters ranged from 1.0 to 5.6 μm. Interestingly, MnO_2-IV nanospheres agglomerated more compactly and smaller than the other three samples, and the surface morphologies of the

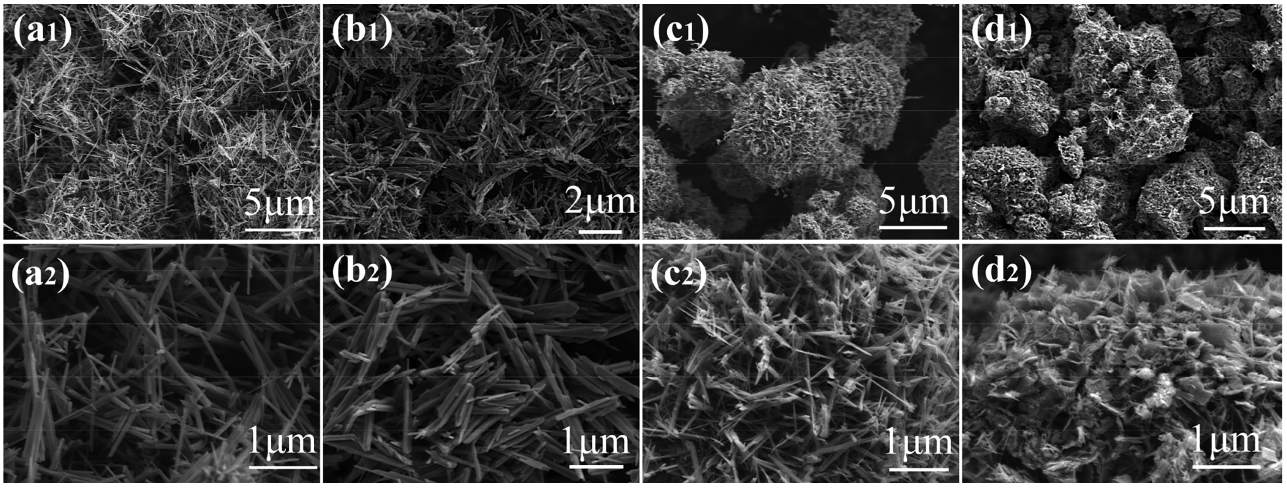

Figure 3. SEM images of (a1,a2) MnO_2-I, (b1,b2) MnO_2-II, (c1,c2) MnO_2-III, and (d1,d2) MnO_2-IV.

https://doi.org/10.1021/acsomega.2c00120
ACS Omega 2022, 7, 9818−9833

particles (Figure. 3h) showed lichen-like or cactus-like structures with many thin flaky protrusions. This should be related to the layered structures of weakly crystalline δ-MnO_2 on the surface,[46] attributed to the intense peak ((003) plane) in its XRD pattern.

The textural properties were investigated by N_2 adsorption−desorption characterization and are summarized in Table 1.

Table 1. Textural Properties of Manganese Oxides

catalyst	BET surface area ($m^2 \cdot g_{cat}^{-1}$)	pore volume[a] ($mL \cdot g_{cat}^{-1}$)	avg. pore diameter[b] (nm)
MnO_2-I	22	7.8	16.9
MnO_2-II	11	3.3	12.9
MnO_2-III	42	17.0	18.0
MnO_2-IV	84	29.5	12.6

[a]BJH desorption cumulative volume of pores. [b]BJH desorption average pore diameter.

Specific surface area and pore volume of the samples decreased in the order of MnO_2-IV > MnO_2-III > MnO_2-I > MnO_2-II. Among them, MnO_2-IV possessed the largest specific surface area of 84 $m^2 \cdot g_{cat}^{-1}$ with the largest pore volume of 29.5 $mL \cdot g_{cat}^{-1}$, which was beneficial to decompose ozone. In comparison, MnO_2-II possessed the lowest specific surface area and pore volume of 11 $m^2 \cdot g_{cat}^{-1}$ and 29.5 $mL \cdot g_{cat}^{-1}$, respectively, possibly resulting in a poor catalytic activity.[38] The detailed nitrogen adsorption−desorption isotherms are shown in Figure S3, and the inset curves in Figure S3 show the pore size distribution calculated by the BJH method. All of these catalysts exhibit type IV isotherms with a H3 hysteresis loop,[38,46] and no obvious saturated adsorption platform was observed. This indicated that these catalysts possessed plentiful mesopores, and the pore structures were very irregular.[47] The average pore size decreased in the order of MnO_2-III > MnO_2-I > MnO_2-II > MnO_2-IV. Specifically, MnO_2-I and MnO_2-II possessed a broad mesopore distribution in the range of 2−20 nm, in particular, concentrated in the range of 2−6 nm, with a slow tail distribution above 20 nm. This led to the very weak hysteresis loop and the low nitrogen adsorption−desorption capacity, corresponding to the low specific surface area. MnO_2-III possessed a broad mesopore distribution in the range of 4−50 nm with a wide peak centered at 15.6 nm and several small peaks below 4 nm. Nevertheless, MnO_2-IV possessed a concentrated mesopore distribution in the range of 3−20 nm with two sharp peaks centered at 3.9 and 6.3 nm and a wide peak centered at 15.5 nm. Given the low proportion of peaks at <4 nm in the curves of MnO_2-III (Figure S3c), the smaller pores observed in MnO_2-IV should be attributed to the tiny gaps formed by the surface cactus-like structure, which could increase the surface reaction area.

3.2. O_3 Decomposition Performance. After determining the basic characteristics of the synthesized catalyst, the ozone decomposition tests were carried out. The ozonation reactor is usually installed upstream of the wet scrubber inlet for flue gas treatment, where the flue gas temperature is around 80−140 °C. Moreover, the original WFGD tower is used as the wet scrubber in most renovation projects and is operated at 40−80 °C to achieve better removal efficiency. Additionally, the wet-plume elimination device is sometimes applied downstream of the wet scrubber outlet to condense, dehydrate, and reheat the flue gas, which further increased the flue gas temperature even over 100 °C.[48] Hence, in order to screen out the catalyst that can effectively decompose ozone at the outlet condition of the wet scrubber, the deO_3 activities of four synthesized MnO_2 under 25−100 °C as well as different GHSV were investigated, and the results are shown in Figure 4. Moreover, the quartz sand (SiO_2) was used as an object of reference to characterize the natural decomposition efficiency of ozone, which was found to be less than 1% below 100 °C and therefore could be ignored here.

As shown in Figure 4a, the ozone decomposition efficiency of these samples increased as flue gas temperature increase when GHSV was set at ∼30000 h^{-1}. The deO_3 activity of MnO_2-II with the smallest specific surface area (11 $m^2 \cdot g_{cat}^{-1}$) and the highest crystallinity was significantly lower than that of the other three, and its deO_3 efficiency only reached 75.86% even at 97 °C. MnO_2-IV with the largest specific surface area (84 $m^2 \cdot g_{cat}^{-1}$) showed the best overall activity. It indicated that the specific surface area had a great influence on the ozone decomposition activity. Nevertheless, the samples except for MnO_2-II exhibited similarly high activities. Specifically, their deO_3 activities at 25 °C were all higher than 90% and decreased in the order of MnO_2-IV (98.75%) > MnO_2-III (97.63%) > MnO_2-I (94.11%), further achieving ∼100% above 60 °C, which was not strictly following their BET sequence. Meanwhile, the gap between their activities was also not as obvious as that in their BET results, suggesting that the catalytic activity was not only determined by BET results. In fact, the specific surface area is just one of the important factors

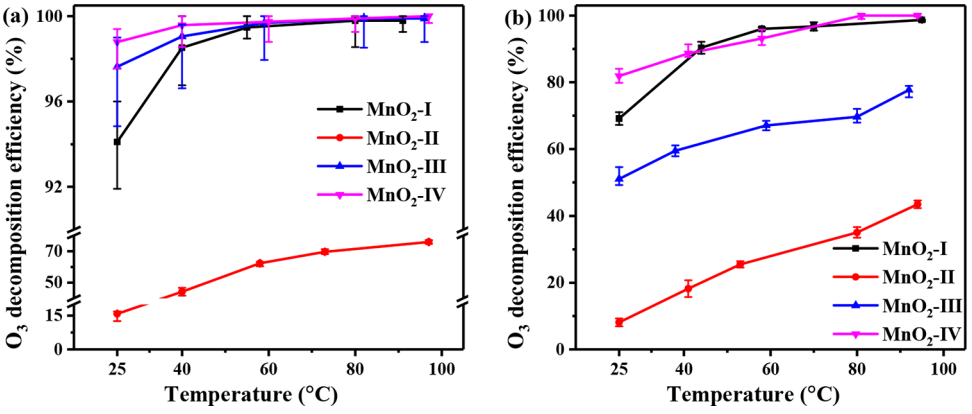

Figure 4. O_3 conversion efficiency over four synthesized MnO_2 at different temperatures when GHSV was set at ∼30000 h^{-1} (a) and ∼90000 h^{-1} (b).

https://doi.org/10.1021/acsomega.2c00120
ACS Omega 2022, 7, 9818−9833

affecting the catalytic activity. Other catalytic properties, such as structure, redox properties, valence states of key elements, etc., also have an impact on its activity. Moreover, it also suggested that the gaps between the above three samples cannot be well-distinguished under the tested conditions. Therefore, the GHSV was further set at ~90000 h^{-1} by reducing the amount of catalyst to make a detailed comparison.

As shown in Figure 4b, a higher GHSV implied that the reactants were in contact with samples for less time, and thus their ozone decomposition efficiency exhibited a significant drop. The activity sequence was MnO_2-IV > MnO_2-I > MnO_2-III > > MnO_2-II. The activity order of MnO_2-I and MnO_2-III was inconsistent with that in Figure 4a, attributed to the difference of their out-diffusion effects. The higher GHSV also promoted a mass transfer coefficient that exhibited a positive impact on chemical reactions. This effect might have a stronger promoting effect on MnO_2-I, thus leading to an obvious gap and a higher deO_3 activity compared to that of MnO_2-III. Overall, MnO_2-I and MnO_2-IV showed excellent ozone decomposition activity, achieving 93.11 and 96.00% at 58 °C, respectively. In addition, the deO_3 efficiency of MnO_2-IV further reached 100% over 81 °C, positively benefiting from its unique cactus-like structure, large specific surface area, and slight lattice defects. Hereby, MnO_2-IV was selected as the material for the subsequent sulfur and water vapor resistance tests.

3.3. TPR/TPD Results. The catalytic activity of ozone decomposition is usually correlated with redox properties, oxygen adsorption−desorption capabilities, and the surface transference of oxygen species, thus H_2-TPR and O_2-TPD experiments were conducted, and the results are shown in Figure 5. Table 2 calculates their total H_2 consumption in the reduction process based on the H_2 uptake of standard copper oxide. As shown in the inset patterns of Figure 5a, the diffraction pattern for MnO_2-I after H_2 reduction under 500 °C exhibited sharp and intense peaks that corresponded to MnO (JCPDS #07-0230),[49] and the same was true for the other samples. This indicated that these peaks in H_2-TPR profiles should be assigned to the reduction of high valence manganese to Mn^{2+}, mainly proceeding along the reduction process of $Mn^{4+} \rightarrow Mn^{3+} \rightarrow Mn^{2+}$,[47] i.e., the multimodal reduction process of $MnO_2 \rightarrow Mn_2O_3 \rightarrow Mn_3O_4 \rightarrow MnO$.[50] Commonly, the peaks below ~300 °C were assigned to the reduction from Mn^{4+} species to Mn^{3+}, and the peaks above 300 °C were assigned to the reduction from Mn^{3+} species in different compound forms to Mn^{2+} species. The amount of H_2 consumption increased in the order of MnO_2-IV < MnO_2-I < MnO_2-III < MnO_2-II, in contrast to their deO_3 activity sequence, and the sample that consumed less H_2 generally exhibited a better deO_3 performance. This indicated that manganese species with lower valence benefitted from ozone decomposition. Moreover, it was notable that MnO_2-IV could be reduced at the lower temperature (corresponding to the first reduction peak centered at 275 °C) and consumed the least amount of hydrogen (8.97 mmol·g_{cat}^{-1}). Hence, MnO_2-IV possessed the best reducibility and the lowest average valence of Mn species, which was beneficial to eliminate ozone effectively.[18]

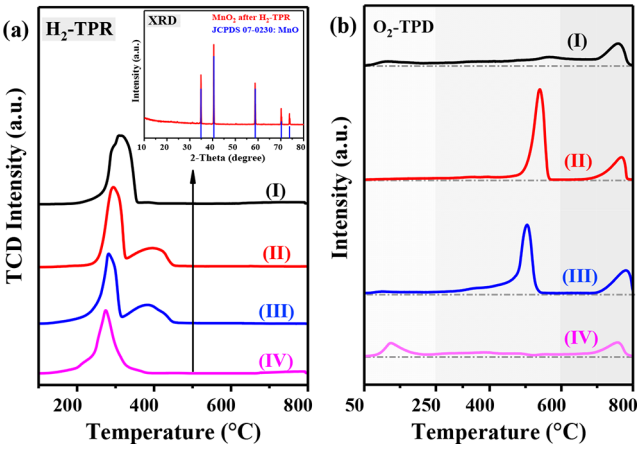

Figure 5. (a) H_2-TPR profiles and (b) O_2-TPD profiles of samples: (I) MnO_2-I, (II) MnO_2-II, (III) MnO_2-III, and (IV) MnO_2-IV. The inset curve shows XRD patterns of MnO_2-IV after 500 °C/TPR reaction.

Table 2. Peak and Hydrogen Consumption in H_2-TPR Profiles over Four Synthesized MnO_2

catalyst	first peak center (°C)	second peak center (°C)	total H_2 consumption (mmol·g_{cat}^{-1})
MnO_2-I	309		11.21
MnO_2-II	329	475	13.08
MnO_2-III	282	383	12.41
MnO_2-IV	275		8.97

It is well-accepted that surface-active oxygen species and oxygen vacancies are important for the process of oxygen adsorption, conversion, and desorption.[51] Therefore, O_2-TPD tests were conducted to investigate the oxygen adsorption−desorption behavior of synthesized MnO_2. As shown in Figure 5b, the desorption peaks below 250 °C were associated with physically adsorbed oxygen. The peaks in the range of 250−600 °C were attributed to the release of the chemically adsorbed oxygen species,[52] as well as part of the subsurface lattice oxygen,[53] while the peaks above 600 °C were attributed to the bulk lattice oxygen species.[54,55] Both MnO_2-IV and MnO_2-I had obvious desorption peaks below 250 °C, which had a relatively good catalytic activity, coinciding with the reported studies that the deO_3 activity was related to the low-temperature oxygen adsorption−desorption properties. Most obviously, MnO_2-IV had the largest low-temperature peak centered at 124 °C and a weak broad peak in the range of 250−530 °C. This reflected that MnO_2-IV possessed an excellent oxygen adsorption capacity, abundant oxygen vacancies, and active oxygen species, beneficial to its excellent catalytic activity. In addition, neither the least active MnO_2-II nor the relatively better active MnO_2-III exhibited almost no oxygen desorption below 250 °C but corresponded to a significant difference in deO_3 activity. This was partly related to the gap of their specific surface areas. Moreover, it suggested that the deO_3 activity of the catalyst was not only determined by its oxygen adsorption−desorption behavior but also affected by various properties of the material. Therefore, a comprehensive measure is required in designing and optimizing catalyst formulations.

3.4. Surface Elements. X-ray photoelectron spectroscopy was used to characterize the oxidation state of Mn and O species, which were highly correlated with catalytic activities. Mn $2p_{3/2}$, O 1s, and Mn 3s XP spectra of the original samples are shown in Figure S4, and those spectra of the spent samples after decomposing ozone are shown in Figure 6. Further, by deconvolution of XPS curves, the details of species

https://doi.org/10.1021/acsomega.2c00120
ACS Omega 2022, 7, 9818−9833

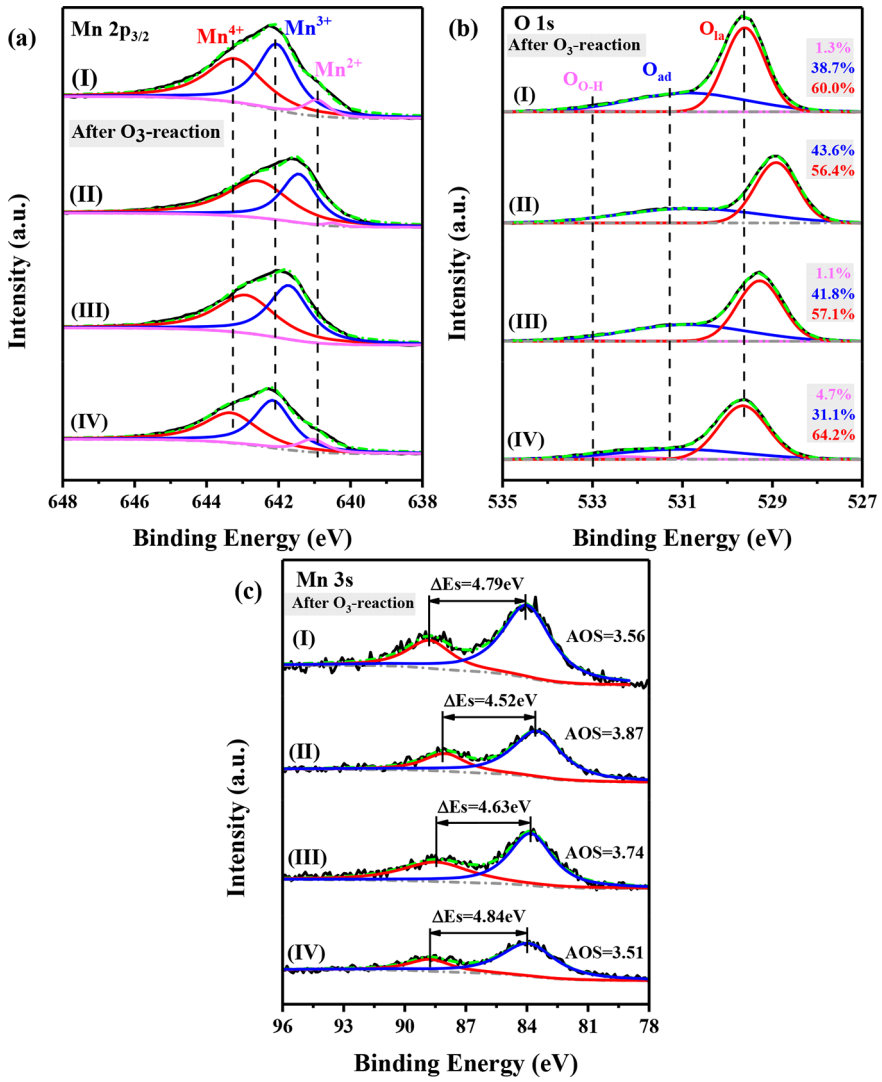

Figure 6. XPS spectra for samples after O_3 decomposition reaction: (a) Mn $2p_{3/2}$, (b) O 1s, and (c) Mn 3s. Samples: (I) MnO_2-I-O_3, (II) MnO_2-II-O_3, (III) MnO_2-III-O_3, and (IV) MnO_2-IV-O_3.

Table 3. XPS Results of Mn 2p and O 1s of MnO_2-I, MnO_2-II, MnO_2-III, MnO_2-IV, and Their Spent Samples

	Mn $2p_{3/2}$					O 1s		
catalyst	Mn^{4+} (%)	Mn^{3+} (%)	Mn^{2+} (%)	$(Mn^{3+} + Mn^{2+})/Mn^{4+}$	AOS	O_{O-H} (%)	O_{ad} (%)	O_{la} (%)
MnO_2-I	40.7	53.5	5.8	1.46	3.69	1.1	40.0	58.9
MnO_2-II	56.8	42.4	0.8	0.76	3.91	0.5	33.6	65.9
MnO_2-III	52.8	46.1	1.1	0.89	3.81	1.1	36.4	62.5
MnO_2-IV	40.6	51.2	8.2	1.46	3.63	1.9	34.2	63.9
MnO_2-I-O_3	46.1	46.4	7.5	1.17	3.56	1.3	38.7	60.0
MnO_2-II-O_3	56.3	42.7	1.0	0.78	3.87	0.0	43.6	56.4
MnO_2-III-O_3	50.5	49.5	0.0	0.98	3.74	1.1	41.8	57.1
MnO_2-IV-O_3	42.8	47.8	9.4	1.34	3.51	4.7	31.1	64.2

concentration ratios and Mn average oxidation state (AOS) were calculated and summarized in Table 3. Mn 3s spectra (Figure 6c) were fitted to two peaks centered at ~89.1 and ~84 eV, and then AOS could be calculated by eq 5,[56] where ΔEs presented the difference in binding energy between the centers of the two peaks.

$$AOS = 8.956 - 1.126\Delta Es \quad (5)$$

As shown in Figure 6a and Figure S4A, the Mn $2p_{3/2}$ spectra centered at ~642 eV were deconvolved to three peaks located at ~640.5, ~642.0, and ~642.7 eV, corresponding to Mn^{2+}, Mn^{3+}, and Mn^{4+} species,[31,57] respectively. The detailed distribution energies of manganese and oxygen species are listed on Table S1. Both the ratio of low valence Mn species ($(Mn^{3+} + Mn^{2+})/Mn^{4+}$) and the calculated AOS (Table 3) decrease in the order of MnO_2-IV > MnO_2-I > MnO_2-III > MnO_2-II, coinciding with their deO_3 performance as well as their H_2 consumption in the H_2-TPR results. Further, MnO_2-IV-O_3 exhibited the lowest manganese AOS (3.51) after the 5 h deO_3 experiments, followed by MnO_2-I-O_3 (3.56) and

https://doi.org/10.1021/acsomega.2c00120
ACS Omega 2022, 7, 9818−9833

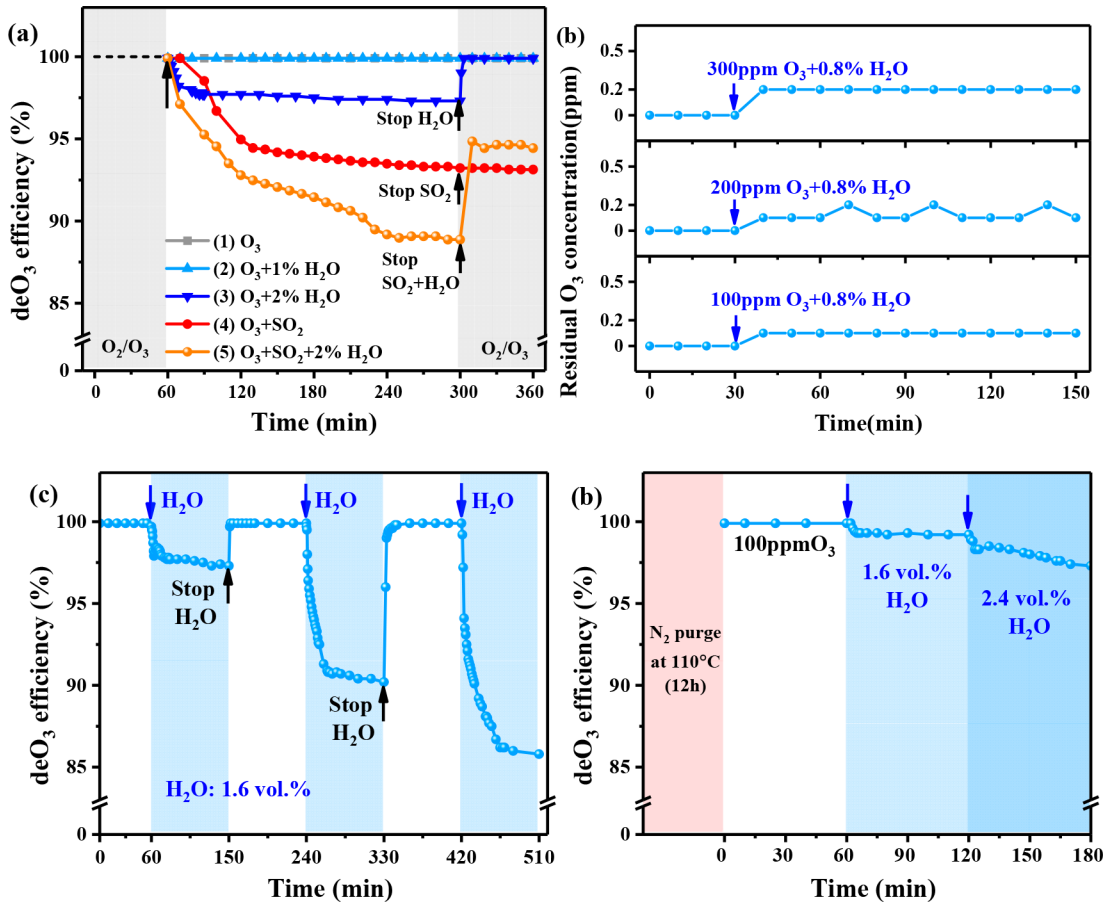

Figure 7. (a) Water vapor and SO_2 interference on ozone decomposition over MnO_2-IV at 80 °C. (b) Ozone concentration interference. (c) Circular deO_3 efficiency under water vapor treatment. (d) deO_3 performance of reactivated MnO_2-IV. Conditions: (1) 100 ppm of O_3; (2) O_3 + 1.0% H_2O; (3) O_3 + 2.0% H_2O; (4) O_3 + 10 ppm of SO_2; (5) O_3 + 10 ppm of SO_2 + 2.0% H_2O.

MnO_2-III-O_3 (3.74). The lower AOS commonly represented more low valence Mn species and more oxygen vacancies,[58] indicating more active centers and higher efficiency in catalytically decomposing ozone.[56,59] Notably, after deO_3 reaction, the proportions of Mn^{3+} species in the spent MnO_2-I and MnO_2-IV decreased from 53.5 to 46.4% and from 51.2 to 47.8%, respectively. Meanwhile, the proportions of Mn^{4+} and Mn^{2+} species were improved. However, the ratios of Mn^{3+} species in MnO_2-II or MnO_2-III that possessed a relatively poor deO_3 activity were approximately unchanged by reacting with ozone. Therefore, it indicated that Mn^{3+} species were the key intermediate factors of the valence transition in the ozone decomposition cycle process. Above all, MnO_2-IV possessed the most oxygen vacancies as well low valence Mn species, thus exhibiting the highest deO_3 activity.

The O 1s spectra of four MnO_2 and their ozone-treated samples are shown in Figure S4B and Figure 6b, respectively. The curves were approximately deconvolved to three peaks located at ∼529.7, ∼531.5, and ∼533 eV, corresponding to lattice oxygen (O_{la}), adsorb oxygen (O_{ad}), and hydroxyl oxygen (O_{O-H}) species,[18,31,57] respectively. As reported, the surface-adsorbed oxygen species exhibits high activities in the oxidation reaction. Obviously, the proportion of oxygen species other than lattice oxygen (Table 3) decreased in the order of MnO_2-I > MnO_2-III > MnO_2-IV > MnO_2-II, hence MnO_2-I with plentiful O_{ad} species exhibited a good deO_3 activity. It also coincided with their deO_3 performance except for MnO_2-IV. Nevertheless, the original MnO_2-IV possessed the highest proportion of hydroxyl oxygen species compared to the others, which should be assessed to the interlayer-adsorbed water in the rich sheet/layer structure on the cactus-like surface. In particular, the proportion of hydroxyl oxygen species in MnO_2-IV had been further improved from 1.9 to 4.7% after ozone treatment, whereas that of the other samples was approximately unchanged. It was deduced that the surface hydroxyl oxygen species also plays an important role in the O_3 decomposition process over MnO_2-IV, which was different from that in MnO_2-I.

3.5. Water Vapor and Sulfur Resistance. Through the above characterization, MnO_2-IV possessed the largest specific surface area, the best low-temperature reducibility, and the most low valence Mn species, oxygen vacancies, and hydroxyl oxygen species, resulting in the highest catalytic activity. However, even if the stringent ultralow emission standard (SO_2 < 35 mg/Nm^3) was met, residual SO_2 after the wet scrubber would also cause sulfur poisoning.[11] Further, the nearly saturated water vapor in the flue gas also had an uncertain impact on the catalyst. Therefore, the resistance tests to H_2O and SO_2 were subsequently conducted over MnO_2-IV to investigate its performance in the complex flue gas condition, and the results are shown in Figure 7. The moisture humidity in the simulated flue gas was changed by adjusting the ratio of N_2 flow through the bubbling−evaporation device, and the concentration of SO_2 in the sulfur resistance experiment was set at ∼10 ppm (approximately equal to 30 mg/Nm^3).

https://doi.org/10.1021/acsomega.2c00120
ACS Omega 2022, 7, 9818−9833

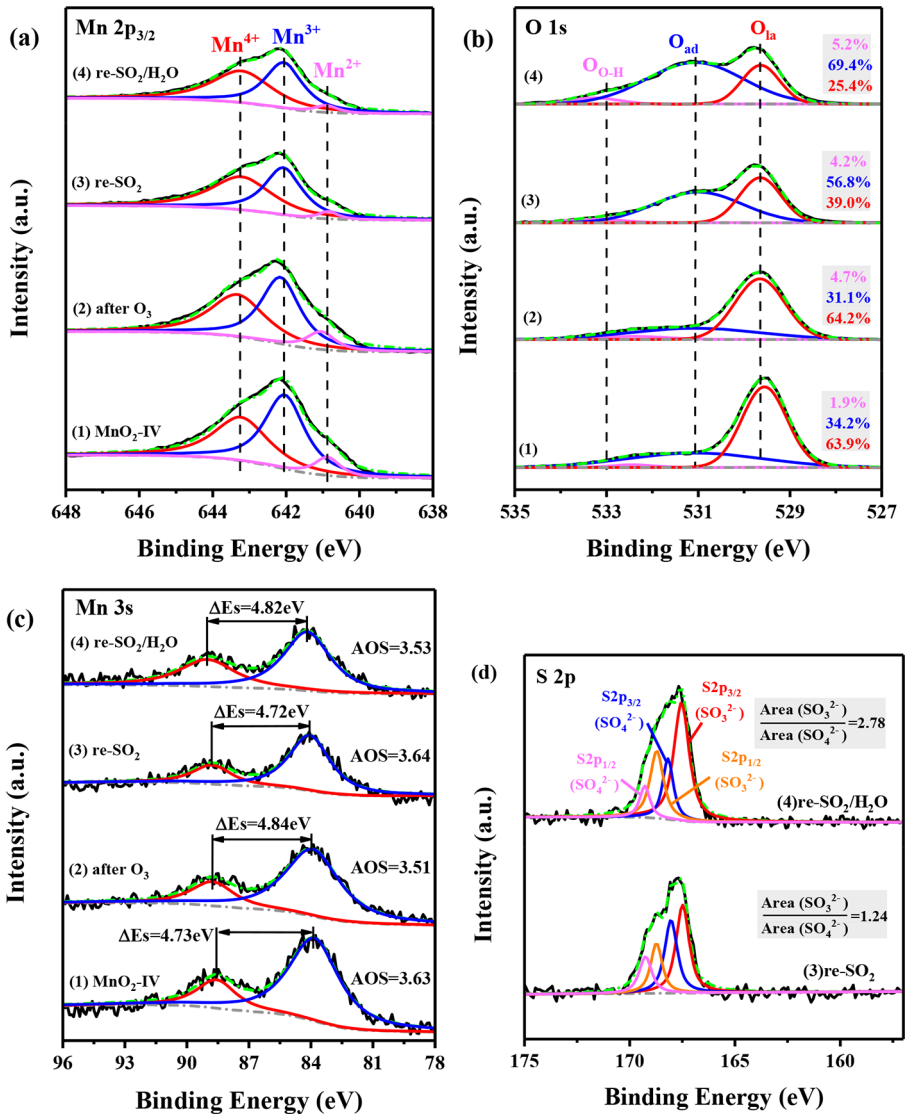

Figure 8. XPS spectra for samples after SO_2/H_2O resistance tests: (a) Mn $2p_{3/2}$, (b) O 1s, (c) Mn 3s, and (d) S 2p. Samples: (1) MnO_2-IV, (2) MnO_2-IV-O_3, (3) MnO_2-IV-O_3/SO_2, and (4) MnO_2-IV-$O_3/SO_2/H_2O$.

3.5.1. Catalytic Activity under $H_2O/SO_2/(SO_2 + H_2O)$. The deO_3 activities of MnO_2-IV in H_2O/SO_2 resistance tests at 80 °C are shown in Figure 7a. Obviously, the decomposition efficiency could maintain at ∼100% in the low-humidity condition (∼1.0% H_2O). In addition, the outlet ozone concentration was less than 0.2 ppm (Figure 7b), even increasing the initial O_3 concentration to 300 ppm, which exhibited good tolerance to low concentration water vapor. As water vapor concentration was increased to ∼2.0%, the deO_3 efficiency decreased and finally stabilized at ∼97.0% within the 240 min test. Interestingly, its efficiency rapidly turned back to ∼100% after stopping the bubbling. It suggested that excess H_2O possibly competed with O_3 molecules for the surface-active sites on MnO_2-IV.[14,56] Specifically, H_2O molecules would be adsorbed and desorbed at the sites, and the dynamic process should be affected by temperature, GHSV, and O_3/H_2O concentration, etc. Herein, when the H_2O molecule achieved the adsorption−desorption equilibrium under a low humidity, the unoccupied active sites were sufficient to decompose O_3, thus the deO_3 efficiency could be stable at 100%. However, after increasing to an unbearable humidity, the left active sites could not decompose ozone completely, and thus the slight deactivation occurred.

To further reveal the interference of water vapor, a lasting circular test was conducted on MnO_2-IV by a periodic H_2O treatment, and the deactivation−reactivation curves are shown in Figure 7c. It is notable that the deO_3 efficiency could always be restored to ∼100% after switching to dry gas flow. It indicated that the effect of adsorption−desorption water vapor on the active sites was slight and even partially reversible. Therefore, its deO_3 efficiency could gradually recover to ∼100% as the desorption process of H_2O molecules with the release of surface sites. However, the deO_3 activity decreased to the level of the former cycle quickly once switching to wet gas flow and exhibited more and more deactivation in the wet−dry cycle. This was because only part of the physically adsorbed H_2O molecules could be desorbed by simply switching to dry gas flow below 100 °C. The incomplete desorption released the partial active sites, and this effect was cumulative, corresponding to the equilibrium of competitive adsorption. Hence, H_2O molecules would compete with O_3 molecules for the remaining active sites in the next switch of

https://doi.org/10.1021/acsomega.2c00120
ACS Omega 2022, 7, 9818−9833

Table 4. XPS Results of Mn 2p and O 1s of MnO_2-IV and the Spent Samples after $O_3/SO_2/H_2O$ Treatment

	Mn $2p_{3/2}$					O 1s		
catalyst	Mn^{4+} (%)	Mn^{3+} (%)	Mn^{2+} (%)	$(Mn^{3+} + Mn^{2+})/Mn^{4+}$	AOS	O_{O-H} (%)	O_{ad} (%)	O_{la} (%)
MnO_2-IV	40.6	51.2	8.2	1.46	3.63	1.9	34.2	63.9
MnO_2-IV-O_3	42.8	47.8	9.4	1.34	3.51	4.7	31.1	64.2
MnO_2-IV-O_3/SO_2	51.2	45.1	3.7	0.95	3.49	4.2	56.8	39.0
MnO_2-IV-$O_3/SO_2/H_2O$	49.9	45.8	4.3	1.00	3.53	5.2	69.4	25.4

wet gas flow, resulting in a faster and more serious deactivation. After being dried under vacuum and purged via N_2 flow, the active sites occupied by physically adsorbed H_2O molecules could be fully released. In addition, the slight changes in the bulk phase of MnO_2-IV excited more oxygen vacancies in O_3-H_2O deactivation−reactivation loops.[30] Thus, the water vapor tolerance of spent MnO_2-IV (Figure 7d, 110 °C, 12 h) was even better than that of the untreated sample.

In the sulfur resistance experiment, the catalyst quickly deactivated with the introduction of SO_2, and its deO_3 efficiency finally slowly decreased to 93.3%. Moreover, the catalytic efficiency could hardly recover after stopping SO_2, and even incessantly dropped to 93.1%. In brief, SO_2 would compete with O_3 molecules for surface active sites,[60] as H_2O molecules did. The initial rapid decline in the deO_3 activity could be attributed to the low resistance of the competition between SO_2 and O_3 molecules during the initial poisoning. As the adsorption−desorption equilibrium (like H_2O molecules) was approached, the resistance increased and so the deactivation rate gradually went slowly. Moreover, the formed sulfates/sulfites could not be decomposed at 80 °C and further blocked the active centers, leading to the irreversible deactivation. Therefore, although MnO_2-IV maintained the deO_3 efficiency of over 90% within the 300 min sulfur resistance experiment, the optimization and improvement were necessary for the actual project application containing SO_2.

Regarding the synergistic interference of water vapor and SO_2, the catalytic activity of MnO_2-IV exhibited a larger decreasing trend and amplitude compared to that affected by any single factor, and the efficiency eventually tended to 88.9%. Similar to the phenomenon in our previous research,[18] it suggested that more serious deactivation had occurred under the synergistic interference of H_2O and SO_2, corresponding to the simultaneous competitive adsorption of H_2O/SO_2 molecules as well as the irreversible reaction. Nevertheless, the deO_3 efficiency could recover to 94.5% after stopping H_2O/SO_2, which was between the efficiency affected by SO_2 alone and that affected by H_2O alone. It suggested that the deactivation was partially recoverable; that is, the synergistic effect of H_2O/SO_2 alleviated the irreversible sulfur poisoning. On one hand, H_2O molecules occupied some active sites in the competitive adsorption process and blocked the irreversible reaction caused by SO_2 to some extent. On the other hand, H_2O molecules probably promoted the formation of unstable sulfate/sulfite species that could be decomposed, thus reducing the poisoning after reactivation.

3.5.2. Catalytic Characterization of the H_2O/SO_2-Treated Samples. XRD patterns of MnO_2-IV, MnO_2-IV-O_3/SO_2, and MnO_2-IV-$O_3/SO_2/H_2O$ (Figure S5) showed that the effect of sulfur led to a weaker diffraction peak at 12.4° (003 plane) and a slight broader band centered at 25.0° (006 plane). Moreover, the synergistic effect of sulfur and water further weakened the peaks at 12.4, 25.0, and 37.1° (012 plane). It indicated that the poisoning process possibly changed the bulk phase slightly. Further, the broadening of the peak centered at 25.0° was suppressed under the interference of H_2O, corresponding to the irreversible poisoning probably. The XPS results of Mn $2p_{3/2}$, O 1s, Mn 3s, and S 2p in the spent MnO_2-IV are shown in Figure 8. Moreover, the details were calculated by deconvolution of XPS curves and are summarized in Table 4, where the abbreviated sample (i.e., MnO_2-IV-$O_3/SO_2/H_2O$) presented the spent MnO_2-IV experienced sulfur and water resistance tests. As shown in Figure 8a,c and Table 4, the ratio of low valence Mn species in MnO_2-IV-O_3/SO_2, especially that of Mn^{2+} species, was significantly reduced after sulfur poisoning and was converted into Mn^{4+} species. However, the above conversion of Mn^{2+} and Mn^{3+} species was weakened by water vapor. The proportion of $(Mn^{3+} + Mn^{2+})/Mn^{4+}$ decreased in the order of MnO_2-IV-O_3 > MnO_2-IV-$O_3/SO_2/H_2O$ > MnO_2-IV-O_3/SO_2, coinciding with their catalytic performance. This suggested that SO_2 could promote the irreversible oxidation of low valence Mn species, whereas H_2O could inhibit this trend. Thus, MnO_2-IV-O_3/SO_2, which suffered from severe sulfur poisoning, had the highest AOS, followed by MnO_2-IV-$O_3/SO_2/H_2O$, which underwent slight sulfur poisoning.

Further, as shown in Figure 8b, the ratio of the lattice oxygen in the samples decreased significantly after sulfur poisoning. This could be attributed to the transformation from manganese oxides to manganese sulfate/manganese sulfite. Moreover, the ratio of hydroxyl oxygen species of the spent samples was generally higher than that for the original MnO_2-IV and further that in the MnO_2-IV-$O_3/SO_2/H_2O$ was higher than the others, indicating that H_2O molecules could promote the formation of surface-active hydroxyl oxygen species via decomposing ozone process.

The S 2p spectra were fitted by deconvolution, as shown in Figure 8d, the effect of spin−orbit splitting could be observed for sulfur compounds. The binding energy difference between S $2p_{1/2}$ and S $2p_{3/2}$ peak was held at ∼1.2 eV, and the area ratio was fixed at 0.5.[61] The peaks were located at 167.54 and 168.18 eV, corresponding to the S $2p_{3/2}$ peak of SO_3^{2-} and the S $2p_{3/2}$ peak of SO_4^{2-}, respectively.[62] Further, the area ratio of SO_3^{2-} to SO_4^{2-} in MnO_2-IV-O_3/SO_2 was 1.24, whereas that ratio in MnO_2-IV-$O_3/SO_2/H_2O$ was higher than the former, ∼2.78. Obviously, more sulfite species were formed under the promotion of water vapor, consistent with the analysis in section 3.5.1. It could be concluded that in the high-humidity sulfur-containing condition, water vapor would promote the combination with SO_2 and tend to generate more sulfites on the active sites, thereby aggravating the deactivation. After water vapor and SO_2 was stopped, part of the active sites occupied by H_2O molecules could be released. Further, the degradable, desorbed sulfites originating from the interference of H_2O molecules could be partially decomposed, whereas sulfate could not, inhibiting irreversible sulfur poisoning accordingly. As a result, the catalyst activity rose to a value

https://doi.org/10.1021/acsomega.2c00120
ACS Omega 2022, 7, 9818−9833

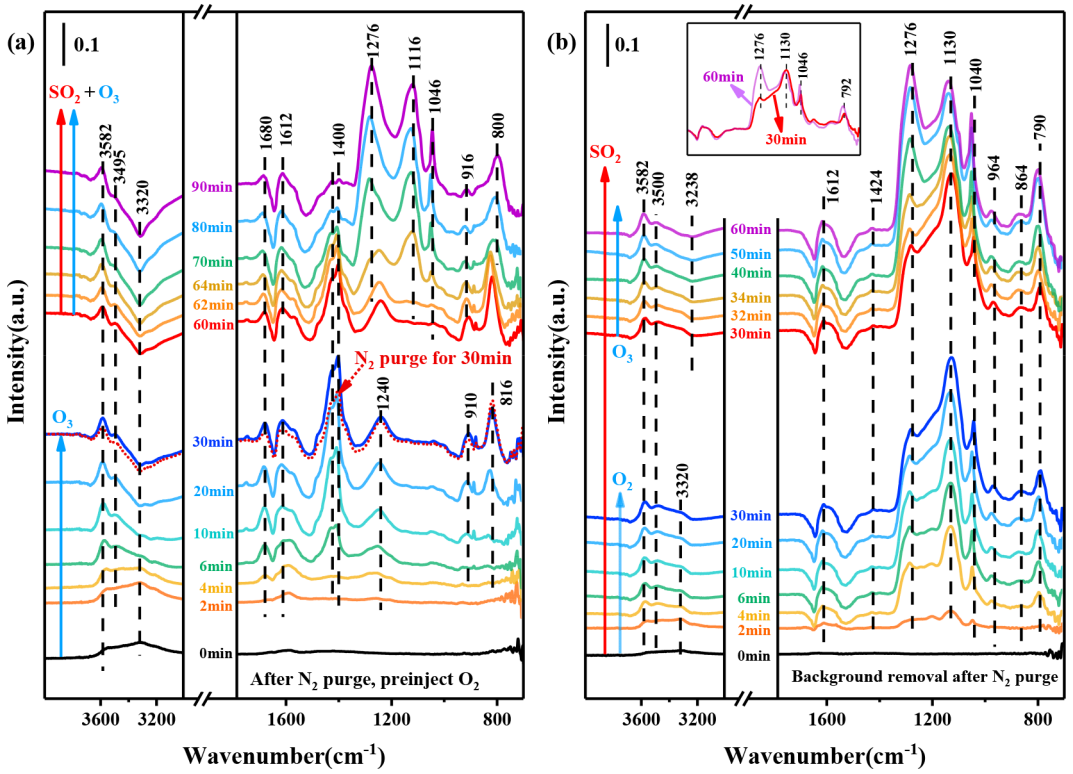

Figure 9. In situ DRIFT spectra of MnO_2-IV exposed to (a) $O_2-O_3-SO_2$ and (b) $(SO_2+O_2)-O_3$ in sequence.

higher than that under the effect of SO_2 alone, but that could not be recovered completely.

3.6. In Situ DRIFTS Study. In situ DRIFTS was conducted to reveal surface intermediates in ozone decomposition process, and the interference of SO_2/H_2O was also investigated. In order to obtain specific information about the adsorption of $O_2/O_3/SO_2/H_2O$ molecules on MnO_2-IV, the different gas components were introduced in sequence balanced with nitrogen.

3.6.1. $O_2-O_3-SO_2$ (the Order of Injected Gas). The tests were marked based on the order of injecting gas as "$O_2-O_3-SO_3$" and "$(SO_2+O_2)-O_3$", where the (SO_2+O_2) presented the co-injection of SO_2 and O_2. As shown in Figure 9a, the background was collected after N_2 flow purge, and then O_2 was preinjected with N_2 as the balance gas. The spectra of 0 min in Figure 9a correspond to the introduction of ozone (~200 ppm). The broad weak band located at ~3320 cm^{-1} could be ascribed to the extensional vibration of O−H groups from interlayer bound water, and the band at 1680−1610 cm^{-1} characterized the bending mode of adsorbed water.[63,64] As O_3 was injected, the above bands became weaker slowly, and the small band peaks at ~3740 cm^{-1} correspond to the mono-coordinated hydroxyl groups (i.e., surface free hydroxyl). The centered peaks at ~3582 cm^{-1} were assigned to the O−H stretching modes from adsorbed H_2O, two-coordinated OH species (i.e., a doubly bridging hydroxyl group), etc.[65,66] Accordingly, the associated interlayer water and adsorbed water were converted into highly active hydroxyl groups by ozone and active oxygen species, and then hydroxyl groups could participate in ozone decomposition, verifying the XPS results (section 3.5.2).

The adsorption intensity of the above intermediates increased with time after ozone injection and tended to stabilize until the surface was saturated. The bands in the region of 950−600 cm^{-1} were generally ascribed to the lattice vibration of metal oxides,[63] e.g., the adsorbed peroxide (O_2^{2-}) on oxide surfaces generated via ozone.[67] Further, the broad bands centered at 1400, 1240, and ~800 cm^{-1} should be ascribed to the adsorbed oxygen/ozone species linked to the MnO_2-IV surface.[33] Specifically, the intermediate at 1400 cm^{-1} should be assigned to atomic oxygen attached to the strong Lewis acid sites, which was considered to be the main deO_3 active sites on natural zeolite.[68] Nevertheless, there was also research that shows this intermediate was the cause, resulting in the sustained deactivation in the deO_3 process over the ε-MnO_2 catalyst.[55] Therefore, the sample was subsequently purged in N_2 flow for another 30 min to determine the roles of the above species in the deO_3 process over MnO_2-IV. Interestingly, except for the band at ~1400 cm^{-1}, there was almost no drop in the other ozone-related intermediate peaks. It indicated that this intermediate could be partially transformed or decomposed on MnO_2-IV, resulting in its excellent catalytic performance accordingly.

After the injection of O_3 and SO_2, the intensities of the bands at 1240 and 1400 cm^{-1} decreased significantly. Meanwhile, the bands in the range of 1275−1240 cm^{-1} were enhanced, which were commonly attributed to the characteristic vibration peak of bisulfate (HSO_4^-) species.[69] Finally, three strong bands at ~1276, ~1116, and 1046 cm^{-1} were observed, corresponding to bidentate sulfate, chelating sulfate,[70] and sulfite species, respectively. This suggested that the ozone-related intermediates were converted into more stable sulfate/sulfite species in SO_2-containing gas flow, thus leading to the continuous deactivation of the catalyst. In addition, the bands at 910 and 816 cm^{-1} also shrunk and shifted slightly, confirming the activity analysis that the crystal lattice of manganese oxide was changed in the sulfur poisoning process.

https://doi.org/10.1021/acsomega.2c00120
ACS Omega 2022, 7, 9818−9833

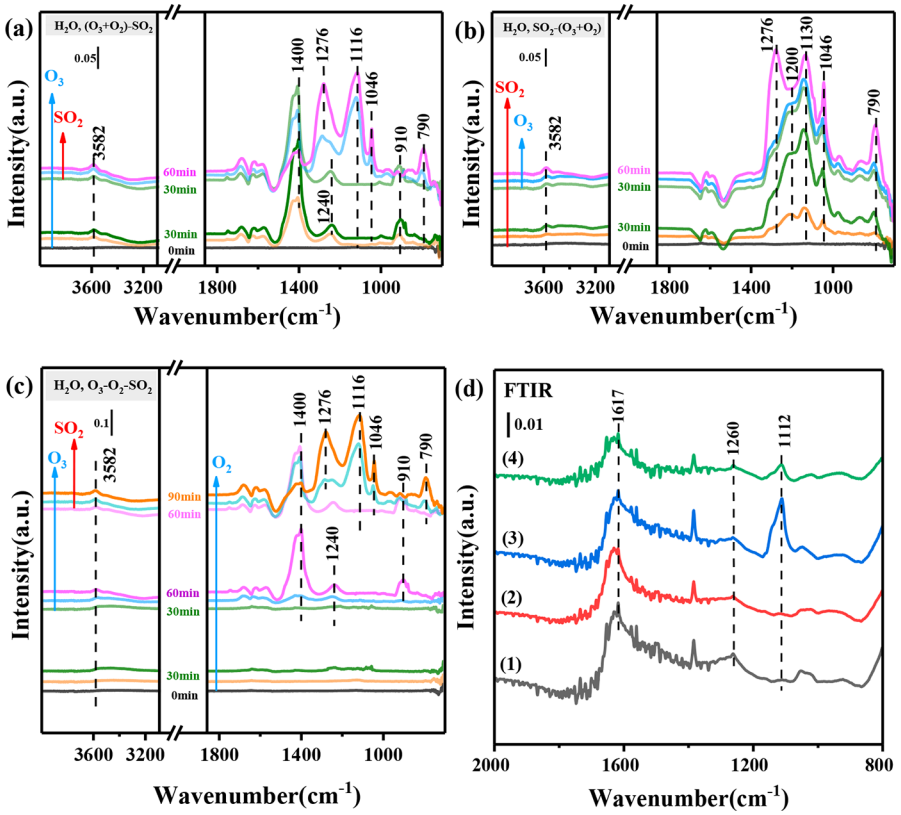

Figure 10. In situ DRIFT spectra of MnO_2-IV after H_2O pretreatment exposed to (a) $(O_3+O_2)-SO_2$, (b) $SO_2-(O_2+O_3)$, and (c) $O_2-O_3-SO_2$ in sequence. (d) FTIR spectra of (1) MnO_2-IV, (2) MnO_2-IV-O_3, (3) MnO_2-IV-SO_2, and (4) MnO_2-IV-SO_2/H_2O.

3.6.2. $(SO_2+O_2)-O_3$. The coadsorption DRIFTS of (SO_2+O_2) was conducted to further distinguish the adsorbed species related to SO_2, and the spectra are shown in Figure. 9b. The bands at 1276, 1130, and 1040 cm^{-1} were also observed after the coadsorption of SO_2 and O_2, which had a little shift compared to those in the $O_2-O_3-SO_2$ test (section 3.6.1). Notably, SO_2 molecules would occupy the surface-active sites after coadsorption and even form sulfate/sulfite species, which further hindered the adsorption−decomposition of O_3. In addition, as shown in the inset curve of Figure 9b, the intensity of the band at 1276 cm^{-1} was significantly improved after ozone injection. This indicated that more sulfate species were accumulated on the surface. There was little change in intensity of the band at 1130 cm^{-1}, which was attributed to this stable sulfate species, hardly affected by ozone. However, the band at 1046 cm^{-1} was assigned to the unstable sulfite species and became weaker as well as those bands ascribed to the lattice vibration, part of which were further converted to sulfate species by strong-oxidizing ozone. Therefore, it caused a sustained slow deactivation of MnO_2-IV, consistent with the results in Figure 7 and Figure 8.

In addition, after ozone injection, the band of bound water exhibited a smaller drop than that in the $O_2-O_3-SO_2$ condition, and the bands of active hydroxyl groups were also weaker. This indicated that SO_2 possibly inhibited the generation of OH species from the reaction between ozone and bound water, thereby reducing the catalytic activity.

3.6.3. Interference of H_2O on Ozone Decomposition. Bound water and active hydroxyl groups played a key role in the deO_3 process. Therefore, in situ H_2O interference DRIFTS experiments were conducted to further reveal the mechanism of water in the decomposition process. Given the water tolerance of the in situ reactor and the measurement interference, MnO_2-IV was fully preadsorbed with H_2O via bubbling before the continuous online detection. According to the order of injected gas, the tests were marked as "H_2O, $(SO_2+O_2)-O_3$", "H_2O, $SO_2-(O_2+O_3)$", and "H_2O, $O_2-O_3-SO_3$", where the (SO_2+O_2) presented the co-injection of SO_2 and O_2.

The conditions and procedures in Figure 10a were similar to those in Figure 9a, except for the water vapor preadsorption. Most obviously, the band at 790 cm^{-1} ascribed to the metal−oxygen bond was not observed after ozone injection. Further, the intensities of the broad bands at ∼3250 cm^{-1} were obviously decreased, which represented the decrease of bound water. The band at ∼3600 cm^{-1} corresponding to the hydroxyl species was strengthened. This suggested that H_2O molecules were bonded on MnO_2-IV after water vapor preadsorption and thus hindered the combination between O_3 molecules with surface oxygen vacancies, coinciding with the results of section 3.5.1. Meanwhile, the bound water was dissociated to surface active hydroxyl species by ozone. Interestingly, MnO_2-IV could still maintain an over 90% deO_3 efficiency in the H_2O resistance experiment (Figure 7), but the intensities of the metal−oxygen bond (e.g., 790 cm^{-1}) had little change. Thus, O_3 molecules are probably bound to the surface-active hydroxyl species as well as H_2O molecules, which had been adsorbed on the active sites.[30] Subsequently, the association intermediates underwent the deO_3 reaction. In other words, O_3 molecules could be decomposed utilizing the surface-active hydroxyl species over MnO_2-IV, instead of being decomposed via oxygen vacancies, which was different from the classic mechanism. In addition, excess H_2O molecules are possibly associated with the adsorbed H_2O molecules by hydrogen

https://doi.org/10.1021/acsomega.2c00120
ACS Omega 2022, 7, 9818−9833

bonds and even formed water film to cover the catalyst, resulting in the recoverable deactivation.

3.6.4. Interference of H_2O on Sulfur Poisoning. As shown in Figure 10b, after oxygen injection, a relatively large weak broad band in the range of 3200−3600 cm^{-1} was observed after SO_2 was injected. It should be attributed to the reaction of SO_2 with the bound water/adsorbed water, accompanying by the formation of a few hydroxyl species. For the synergistic effect of SO_2 and H_2O, the band of the SO_2-related species on the H_2O-pretreated sample, especially the band at 1276 cm^{-1} (ascribed to the stable sulfate species), was relatively weaker than that in Figure 9b. Further, the injected ozone promoted the formation of stable sulfate species, similar to the tests in Figure 9. However, comparing Figure 9a with Figure 10a and Figure 10c, it should be noticed that the intensity of the above sulfate species (1276 cm^{-1}) on the H_2O-pretreated sample was relatively weaker than that of other species (the bands at 1116 and 1046 cm^{-1}). Furthermore, as shown in Figure 10d, the FTIR result of MnO_2-IV-SO_2/H_2O exhibited a weaker peak than with MnO_2-IV-SO_2. The above results indicated that the abundant bound water (or active hydroxyl species) could inhibit the formation of stable sulfate species on MnO_2-IV, which further confirmed the conclusions of H_2O/SO_2 resistance tests (section 3.5.1) and S 2p XP spectra (Figure 8d).

3.6.5. deO_3 Mechanism under Water Interference. Based on the above findings, the mechanism of O_3 molecules being decomposed via bound water and surface-active hydroxyl over MnO_2-IV was proposed. The theoretical diagram is shown in Figure 11, where [o] represents oxygen vacancy and HO• represents surface free hydroxyl. As a comparison, the diagram of the widely reported deO_3 mechanism on oxygen vacancies is shown in Figure S6. The detailed steps are shown in Table 5, where −OH, $-HO_2^-$, and $-O_2^{2-}$ represent surface-active species/intermediates.

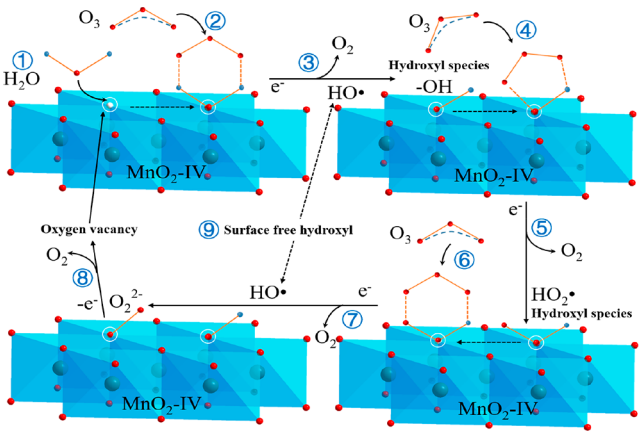

Figure 11. DeO_3 mechanism over MnO_2-IV by bound water and surface-active hydroxyl species. The white, red, blue, and green balls represent oxygen vacancy, O atom, H atom, and Mn atom, respectively.

First, the injected H_2O molecules and interlayer water were adsorbed or transferred to surface-active oxygen vacancies (following step 1). After the stimulation of ozone, the associated H_2O molecules and adsorbed water were converted into highly active hydroxyl groups. Moreover, O_3 molecules were combined with surface-associated H_2O molecules (step 2) and surface-active hydroxyl (steps 4 and 6). Subsequently, the intermediates were decomposed into surface free hydroxyl, hydroxyl species, active oxygen, peroxide species, and oxygen (steps 3, 5, 7, and 8). The surface free hydroxyl excited via the decomposition process could be decomposed into water and oxygen (step 9) or be associated with oxygen vacancies and further participate in the deO_3 reaction, meanwhile providing electrons for steps 3, 5, and 7.

Table 5. Specific Reactions of Ozone Decomposition over MnO_2-IV under Water Interference

reactions under water interference	step
$[o] + H_2O \rightarrow H_2O{-}[o]$	1
$H_2O{-}[o] + O_3 \rightarrow O_3{-}H_2O{-}[o]$	2
$O_3{-}H_2O{-}[o] + e^- \rightarrow [o]{-}OH + HO\bullet + O_2$	3
$[o]{-}OH + O_3 \rightarrow [o]{-}OH{-}O_3$	4
$[o]{-}OH{-}O_3 + e^- \rightarrow [o]{-}HO_2^- + O_2$	5
$[o]{-}HO_2^- + O_3 \rightarrow [o]{-}HO_2^-{-}O_3$	6
$[o]{-}HO_2^-{-}O_3 + e^- \rightarrow [o]{-}O_2^{2-} + HO\bullet + O_2$	7
$[o]{-}O_2^{2-} \rightarrow [o] + O_2 + 2e^-$	8
$2HO\bullet \rightarrow H_2O + 0.5O_2 + 2e^-$	9

4. CONCLUSION

In this work, four manganese oxides with different crystals were hydrothermally synthesized for the decomposition of residual ozone in the ozone synergistic-oxidation system. The synthesized MnO_2 and their spent samples were systematically characterized by XRD, SEM, BET, XPS, H_2-TPR, O_2-TPD, FTIR, and in situ DRIFTS. The specific conclusions are listed in the following:

(i) Cactus-like MnO_2-IV nanospheres possess unique δ-MnO_2-layered morphology, high specific surface area, superior redox properties, oxygen chemisorption capabilities, abundant surface-active hydroxyl species, and low valence Mn species.

(ii) MnO_2-IV exhibited the highest ozone decomposition activity, achieving ∼100% efficiency at 40−100 °C. It also showed the excellent tolerance to SO_2/H_2O, which could maintain over 88% deO_3 efficiency in the sulfur-containing high-humidity condition.

(iii) O_3 molecules could be bound to the surface-active hydroxyl species as well as the adsorbed H_2O molecules. Subsequently, the association intermediates could undergo the deO_3 reaction over MnO_2-IV, instead of being directly decomposed on oxygen vacancies. In addition, excess H_2O molecules possibly associated with the adsorbed H_2O molecules by hydrogen bonds and even formed water film to cover the catalyst, resulting in the recoverable deactivation.

(iv) The deactivation caused by SO_2 was irreversible. Further, the synergistic effect of SO_2/H_2O promoted the formation of unstable sulfate species, thereby deepening the deactivation but inhibiting the irreversible poisoning.

■ ASSOCIATED CONTENT

Supporting Information

The Supporting Information is available free of charge at https://pubs.acs.org/doi/10.1021/acsomega.2c00120.

Stability activities of MnO_2-IV, standard XRD patterns, N_2 adsorption/desorption isotherms, XPS spectra, XRD

https://doi.org/10.1021/acsomega.2c00120
ACS Omega 2022, 7, 9818−9833

patterns of spent MnO_2-IV, deO_3 mechanism on oxygen vacancies, and detailed data of XPS results (PDF)

AUTHOR INFORMATION

Corresponding Author

Zhihua Wang − *State Key Laboratory of Clean Energy Utilization, Zhejiang University, Hangzhou 310027, P.R. China;* orcid.org/0000-0002-7521-2900; Email: wangzh@zju.edu.cn

Authors

Hairong Tang − *State Key Laboratory of Clean Energy Utilization, Zhejiang University, Hangzhou 310027, P.R. China;* orcid.org/0000-0001-8935-593X

Jiaming Shao − *State Key Laboratory of Clean Energy Utilization, Zhejiang University, Hangzhou 310027, P.R. China; Zhejiang SUPCON Technology Co., Ltd., Hangzhou 310053, P.R. China*

Fawei Lin − *School of Environmental Science and Engineering, Tianjin University, Tianjin 300072, P.R. China;* orcid.org/0000-0001-5461-8277

Peixi Liu − *State Key Laboratory of Clean Energy Utilization, Zhejiang University, Hangzhou 310027, P.R. China*

Yong He − *State Key Laboratory of Clean Energy Utilization, Zhejiang University, Hangzhou 310027, P.R. China;* orcid.org/0000-0002-7037-9007

Yanqun Zhu − *State Key Laboratory of Clean Energy Utilization, Zhejiang University, Hangzhou 310027, P.R. China;* orcid.org/0000-0002-0981-2078

Complete contact information is available at: https://pubs.acs.org/10.1021/acsomega.2c00120

Notes

The authors declare no competing financial interest.

ACKNOWLEDGMENTS

This research was financially supported by the National Natural Science Foundation of China (52125605) and the Fundamental Research Funds for the Central Universities (2021FZZX001-11).

REFERENCES

(1) Hollingsworth, J. W.; Kleeberger, S. R.; Foster, W. M. Ozone and pulmonary innate immunity. *Proc. Am. Thorac Soc.* **2007**, *4* (3), 240−6.

(2) Nuvolone, D.; Petri, D.; Voller, F. The effects of ozone on human health. *Environ. Sci. Pollut Res.* **2018**, *25* (9), 8074−8088.

(3) Kariisa, M.; Foraker, R.; Pennell, M.; Buckley, T.; Diaz, P.; Criner, G. J.; Wilkins, J. R. Short- and Long-Term Effects of Ambient Ozone and Fine Particulate Matter on the Respiratory Health of Chronic Obstructive Pulmonary Disease Subjects. *Arch Environ. Occup H* **2015**, *70* (1), 56−62.

(4) Kim, B.-J.; Kwon, J.-W.; Seo, J.-H.; Kim, H.-B.; Lee, S.-Y.; Park, K.-S.; Yu, J.; Kim, H.-C.; Leem, J.-H.; Sakong, J.; Kim, S.-Y.; Lee, C.-G.; Kang, D.-M.; Ha, M.; Hong, Y.-C.; Kwon, H.-J.; Hong, S.-J. Association of ozone exposure with asthma, allergic rhinitis, and allergic sensitization. *Ann. Allerg Asthma Im* **2011**, *107* (3), 214−219.

(5) Goodman, J. E.; Zu, K.; Loftus, C. T.; Lynch, H. N.; Prueitt, R. L.; Mohar, I.; Shubin, S. P.; Sax, S. N. Short-term ozone exposure and asthma severity: Weight-of-evidence analysis. *Environ. Res.* **2018**, *160*, 391−397.

(6) Pinto, D. M.; Blande, J. D.; Souza, S. R.; Nerg, A.-M.; Holopainen, J. K. Plant Volatile Organic Compounds (VOCs) in Ozone (O_3) Polluted Atmospheres: The Ecological Effects. *J. Chem. Ecol.* **2010**, *36* (1), 22−34.

(7) Wu, R.; Xie, S. Spatial Distribution of Ozone Formation in China Derived from Emissions of Speciated Volatile Organic Compounds. *Environ. Sci. Technol.* **2017**, *51* (5), 2574−2583.

(8) Rekhate, C. V.; Srivastava, J. K. Recent advances in ozone-based advanced oxidation processes for treatment of wastewater- A review. *Chemical Engineering Journal Advances* **2020**, *3*, 100031.

(9) Loeb, B. L.; Thompson, C. M.; Drago, J.; Takahara, H.; Baig, S. Worldwide Ozone Capacity for Treatment of Drinking Water and Wastewater: A Review. *Ozone Sci. Eng.* **2012**, *34* (1), 64−77.

(10) Britigan, N.; Alshawa, A.; Nizkorodov, S. A. Quantification of Ozone Levels in Indoor Environments Generated by Ionization and Ozonolysis Air Purifiers. *J. Air Waste Manage* **2006**, *56* (5), 601−610.

(11) Shao, J.; Xu, C.; Wang, Z.; Zhang, J.; Wang, R.; He, Y.; Cen, K. NO_x reduction in a 130 t/h biomass-fired circulating fluid bed boiler using coupled ozonation and wet absorption technology. *Ind. Eng. Chem. Res.* **2019**, *58* (39), 18134−18140.

(12) Ma, Q.; Wang, Z.; Lin, F.; Kuang, M.; Whiddon, R.; He, Y.; Liu, J. Characteristics of O_3 Oxidation for Simultaneous Desulfurization and Denitration with Limestone-Gypsum Wet Scrubbing: Application in a Carbon Black Drying Kiln Furnace. *Energy Fuels* **2016**, *30* (3), 2302−2308.

(13) Yamamoto, Y.; Yamamoto, H.; Takada, D.; Kuroki, T.; Fujishima, H.; Okubo, M. Simultaneous Removal of NO_x and SO_x from Flue Gas of a Glass Melting Furnace using a Combined Ozone Injection and Semi-dry Chemical Process. *Ozone Sci. Eng.* **2016**, *38* (3), 211−218.

(14) Lin, F.; Wang, Z.; Zhang, Z.; He, Y.; Zhu, Y.; Shao, J.; Yuan, D.; Chen, G.; Cen, K. Flue gas treatment with ozone oxidation: An overview on NO_x, organic pollutants, and mercury. *Chem. Eng. J.* **2020**, *382*, 123030.

(15) Ling, S. H.; Jing, C. Y.; Zhang, L. J. Analysis Flue Gas Denitration Technology for Small and Medium Sized Coal-Fired Industrial Boilers. *AMR* **2015**, *1092-1093*, 810−813.

(16) Lin, F.; Wang, Z.; Ma, Q.; Yang, Y.; Whiddon, R.; Zhu, Y.; Cen, K. Catalytic deep oxidation of NO by ozone over MnO_x loaded spherical alumina catalyst. *Appl. Catal., B* **2016**, *198*, 100−111.

(17) Shao, J.; Yang, Y.; Whiddon, R.; Wang, Z.; Lin, F.; He, Y.; Kumar, S.; Cen, K. Investigation of NO Removal with Ozone Deep Oxidation in Na_2CO_3 Solution. *Energy Fuels* **2019**, *33* (5), 4454−4461.

(18) Shao, J.; Lin, F.; Wang, Z.; Liu, P.; Tang, H.; He, Y.; Cen, K. Low temperature catalytic ozonation of toluene in flue gas over Mn-based catalysts: Effect of support property and SO_2/water vapor addition. *Appl. Catal., B* **2020**, *266*, 118662.

(19) Wang, Z.; Zhou, J.; Zhu, Y.; Wen, Z.; Liu, J.; Cen, K. Simultaneous removal of NO_x, SO_2 and Hg in nitrogen flow in a narrow reactor by ozone injection: Experimental results. *Fuel Process. Technol.* **2007**, *88* (8), 817−823.

(20) Wei, L.; Chen, H.; Wei, Y.; Jia, J.; Zhang, R. Ce-promoted Mn/ZSM-5 catalysts for highly efficient decomposition of ozone. *J. Environ. Sci.* **2021**, *103*, 219−228.

(21) Lian, Z.; Ma, J.; He, H. Decomposition of high-level ozone under high humidity over Mn-Fe catalyst: The influence of iron precursors. *Catal. Commun.* **2015**, *59*, 156−160.

(22) Berman, J. D.; Fann, N.; Hollingsworth, J. W.; Pinkerton, K. E.; Rom, W. N.; Szema, A. M.; Breysse, P. N.; White, R. H.; Curriero, F. C. Health Benefits from Large-Scale Ozone Reduction in the United States. *Environ. Health Perspect.* **2012**, *120* (10), 1404−1410.

(23) Yang, S.; Zhu, Z.; Wei, F.; Yang, X. Carbon nanotubes/activated carbon fiber based air filter media for simultaneous removal of particulate matter and ozone. *Building and Environment* **2017**, *125*, 60−66.

(24) Lin, F.; Zhu, Y.; Xu, C.; Ma, Q.; Wang, Z.; Zhou, J.; Cen, K. Experimental study on residual ozone decomposition in process of multi-pollutants removal by ozone. *J. Zhejiang Univ-Eng. Sci.* **2015**, No. 07, 1249−1254.

(25) Hellén, H.; Kuronen, P.; Hakola, H. Heated stainless steel tube for ozone removal in the ambient air measurements of mono- and sesquiterpenes. *Atmos. Environ.* **2012**, *57*, 35−40.
(26) Namdari, M.; Lee, C.-S.; Haghighat, F. Active ozone removal technologies for a safe indoor environment: A comprehensive review. *Building and Environment* **2021**, *187*, 107370.
(27) Li, X.; Ma, J.; He, H. Recent advances in catalytic decomposition of ozone. *J. Environ. Sci.* **2020**, *94*, 14−31.
(28) Li, W.; Gibbs, G. V.; Oyama, S. T. Mechanism of Ozone Decomposition on a Manganese Oxide Catalyst. 1. In Situ Raman Spectroscopy and Ab Initio Molecular Orbital Calculations. *J. Am. Chem. Soc.* **1998**, *120* (35), 9041−9046.
(29) Liu, Y.; Yang, W.; Zhang, P.; Zhang, J. Nitric acid-treated birnessite-type MnO_2: An efficient and hydrophobic material for humid ozone decomposition. *Appl. Surf. Sci.* **2018**, *442*, 640−649.
(30) Zhu, G.; Zhu, J.; Jiang, W.; Zhang, Z.; Wang, J.; Zhu, Y.; Zhang, Q. Surface oxygen vacancy induced α-MnO_2 nanofiber for highly efficient ozone elimination. *Appl. Catal., B* **2017**, *209*, 729−737.
(31) Yang, W.; Su, Z. a.; Xu, Z.; Yang, W.; Peng, Y.; Li, J. Comparative study of α-, β-, γ- and δ-MnO_2 on toluene oxidation: Oxygen vacancies and reaction intermediates. *Appl. Catal., B* **2020**, *260*, 118150.
(32) Ma, J.; Wang, C.; He, H. Transition metal doped cryptomelane-type manganese oxide catalysts for ozone decomposition. *Appl. Catal., B* **2017**, *201*, 503−510.
(33) Brodu, N.; Manero, M.-H.; Andriantsiferana, C.; Pic, J.-S.; Valdés, H. Role of Lewis acid sites of ZSM-5 zeolite on gaseous ozone abatement. *Chem. Eng. J.* **2013**, *231*, 281−286.
(34) Zhu, G.; Zhu, J.; Li, W.; Yao, W.; Zong, R.; Zhu, Y.; Zhang, Q. Tuning the K^+ Concentration in the Tunnels of α-MnO_2 To Increase the Content of Oxygen Vacancy for Ozone Elimination. *Environ. Sci. Technol.* **2018**, *52* (15), 8684−8692.
(35) Hong, W.; Zhu, T.; Sun, Y.; Wang, H.; Li, X.; Shen, F. Enhancing Oxygen Vacancies by Introducing Na+ into OMS-2 Tunnels To Promote Catalytic Ozone Decomposition. *Environ. Sci. Technol.* **2019**, *53* (22), 13332−13343.
(36) Rao, Y.; Zeng, D.; Cao, X.; Qin, G.; Li, S. Synthesis of doped MnO_x/diatomite composites for catalyzing ozone decomposition. *Ceram. Int.* **2019**, *45* (6), 6966−6971.
(37) Liu, Y.; Zhang, P. Removing Surface Hydroxyl Groups of Ce-Modified MnO_2 To Significantly Improve Its Stability for Gaseous Ozone Decomposition. *J. Phys. Chem. C* **2017**, *121* (42), 23488−23497.
(38) Li, K.; Chen, C.; Zhang, H.; Hu, X.; Sun, T.; Jia, J. Effects of phase structure of MnO_2 and morphology of δ-MnO_2 on toluene catalytic oxidation. *Appl. Surf. Sci.* **2019**, *496*, 143662.
(39) Chen, T.; Dou, H.; Li, X.; Tang, X.; Li, J.; Hao, J. Tunnel structure effect of manganese oxides in complete oxidation of formaldehyde. *Microporous Mesoporous Mater.* **2009**, *122* (1), 270−274.
(40) Wei, C.; Xu, C.; Li, B.; Du, H.; Kang, F. Preparation and characterization of manganese dioxides with nano-sized tunnel structures for zinc ion storage. *J. Phys. Chem. Solids* **2012**, *73* (12), 1487−1491.
(41) Tang, X.; Li, H.; Liu, Z.-H.; Yang, Z.; Wang, Z. Preparation and capacitive property of manganese oxide nanobelt bundles with birnessite-type structure. *J. Power Sources* **2011**, *196* (2), 855−859.
(42) Kim, H.-m.; Saito, N.; Kim, D.-w. Solution Plasma-Assisted Green Synthesis of MnO_2 Adsorbent and Removal of Cationic Pollutant. *Journal of Chemistry* **2019**, *2019*, 7494292.
(43) Li, Z.; Liu, H.; Ruan, H.; Hu, R.; Su, Y.; Hu, Z.; Huang, J. In situ synthesis rodlike MnO_2/reduced graphene oxide composite as anode materials for Li-ion batteries. *Journal of Materials Science: Materials in Electronics* **2017**, *28* (23), 18099−18105.
(44) Huang, X.; Cui, W.; Yu, J.; Lu, S.; Liao, X. Preparation of Mesoporous MnO_2 Catalysts with Different Morphologies for Catalytic Ozonation of Organic Compounds. *Catal. Lett.* **2021**, DOI: 10.1007/s10562-021-03745-y.
(45) Ji, J.; Lu, X.; Chen, C.; He, M.; Huang, H. Potassium-modulated δ-MnO_2 as robust catalysts for formaldehyde oxidation at room temperature. *Appl. Catal., B* **2020**, *260*, 118210.
(46) Zhao, B.; Ran, R.; Wu, X.; Weng, D. Phase structures, morphologies, and NO catalytic oxidation activities of single-phase MnO_2 catalysts. *Appl. Catal., A* **2016**, *514*, 24−34.
(47) Zhang, Z.; Lin, F.; Xiang, L.; Yu, H.; Wang, Z.; Yan, B.; Chen, G. Synergistic effect for simultaneously catalytic ozonation of chlorobenzene and NO over $MnCoO_x$ catalysts: Byproducts formation under practical conditions. *Chem. Eng. J.* **2022**, *427*, 130929.
(48) Wang, L.; Wu, H.; Wang, Q.; Zhou, C.; Zhang, Z.; Yang, H.; Zhou, Y. Emission reduction of condensable particulate matter in ammonia-based desulfurized flue gas by heterogeneous vapor condensation. *Chem. Eng. Process. Process Intensification* **2021**, *167*, 108519.
(49) Cui, Z.; Guo, X.; Li, H. High performance MnO thin-film anodes grown by radio-frequency sputtering for lithium ion batteries. *J. Power Sources* **2013**, *244*, 731−735.
(50) Sun, L.; Zhao, P.; Liu, Y.; Tan, B.; Yu, C.; Feng, N.; Wang, L.; Wan, H.; Guan, G. Enhancing the catalytic activity of MnO_2 via structural phase transition for propane combustion: Promotional role of ionic liquid. *Journal of Environmental Chemical Engineering* **2021**, *9* (6), 106453.
(51) Huang, C.; Ji, Q.; Zhang, H.; Wang, Y.; Wang, S.; Liu, X.; Guo, Y.; Zhang, C. Ru-incorporated Co_3O_4 nanoparticles from self-sacrificial ZIF-67 template as efficient bifunctional electrocatalysts for rechargeable metal-air battery. *J. Colloid Interface Sci.* **2022**, *606*, 654−665.
(52) Xing, X.; Zhao, T.; Cheng, J.; Duan, X.; Li, W.; Li, G.; Zhang, Z.; Hao, Z. Promotional effect of Cu additive for the selective catalytic oxidation of n-butylamine over CeZrOx catalyst. *Chin. Chem. Lett.* **2021**, DOI: 10.1016/j.cclet.2021.09.056.
(53) Su, Z.; Yang, W.; Wang, C.; Xiong, S.; Cao, X.; Peng, Y.; Si, W.; Weng, Y.; Xue, M.; Li, J. Roles of oxygen vacancies in the bulk and surface of CeO_2 for toluene catalytic combustion. *Environ. Sci. Technol.* **2020**, *54* (19), 12684−12692.
(54) Jia, J.; Zhang, P.; Chen, L. Catalytic decomposition of gaseous ozone over manganese dioxides with different crystal structures. *Appl. Catal., B* **2016**, *189*, 210−218.
(55) Hong, W.; Shao, M.; Zhu, T.; Wang, H.; Sun, Y.; Shen, F.; Li, X. To promote ozone catalytic decomposition by fabricating manganese vacancies in ε-MnO2 catalyst via selective dissolution of Mn-Li precursors. *Appl. Catal., B* **2020**, *274*, 119088.
(56) Zhang, Z.; Xiang, L.; Lin, F.; Wang, Z.; Yan, B.; Chen, G. Catalytic deep degradation of Cl-VOCs with the assistance of ozone at low temperature over MnO_2 catalysts. *Chem. Eng. J.* **2021**, *426*, 130814.
(57) Peng, Y.; Si, W.; Li, J.; Crittenden, J.; Hao, J. Experimental and DFT studies on Sr-doped $LaMnO_3$ catalysts for NO_x storage and reduction. *Catalysis Science & Technology* **2015**, *5* (4), 2478−2485.
(58) Chen, G.; Wang, Z.; Lin, F.; Zhang, Z.; Yu, H.; Yan, B.; Wang, Z. Comparative investigation on catalytic ozonation of VOCs in different types over supported MnO_x catalysts. *J. Hazard. Mater.* **2020**, *391*, 122218.
(59) Mo, S.; Zhang, Q.; Li, J.; Sun, Y.; Ren, Q.; Zou, S.; Zhang, Q.; Lu, J.; Fu, M.; Mo, D.; Wu, J.; Huang, H.; Ye, D. Highly efficient mesoporous MnO_2 catalysts for the total toluene oxidation: Oxygen-Vacancy defect engineering and involved intermediates using in situ DRIFTS. *Appl. Catal., B* **2020**, *264*, 118464.
(60) Lin, F.; Wang, Z.; Zhang, Z.; Xiang, L.; Yuan, D.; Yan, B.; Wang, Z.; Chen, G. Comparative investigation on chlorobenzene oxidation by oxygen and ozone over a MnO_x/Al_2O_3 catalyst in the presence of SO_2. *Environ. Sci. Technol.* **2021**, *55* (5), 3341−3351.
(61) Fantauzzi, M.; Rigoldi, A.; Elsener, B.; Atzei, D.; Rossi, A. A contribution to the surface characterization of alkali metal sulfates. *J. Electron Spectrosc. Relat. Phenom.* **2014**, *193*, 6−15.

https://doi.org/10.1021/acsomega.2c00120
ACS Omega 2022, 7, 9818−9833

(62) Kim, S S.; Britcher, L.; Kumar, S.; Griesser, H. J XPS study of sulfur and phosphorus compounds with different oxidation states. *Sains Malaysiana* **2018**, *47* (8), 1913−1922.
(63) Chesalov, Y. A.; Chernobay, G. B.; Andrushkevich, T. V. FTIR study of the surface complexes of *β*-picoline, 3-pyridine-carbaldehyde and nicotinic acid on sulfated TiO_2 (anatase). *J. Mol. Catal. A: Chem.* **2013**, *373*, 96−107.
(64) Wang, Y.; Hu, X.; Guo, T.; Tian, W.; Hao, J.; Guo, Q. The competitive adsorption mechanism of CO_2, H_2O and O_2 on a solid amine adsorbent. *Chem. Eng. J.* **2021**, *416*, 129007.
(65) Luo, L.; LaCoste, J. D.; Khamidullina, N. G.; Fox, E.; Gang, D. D.; Hernandez, R.; Yan, H. Investigate interactions of water with mesoporous ceria using in situ VT-DRIFTS. *Surf. Sci.* **2020**, *691*, 121486.
(66) Katsigiannopoulos, D.; Grana, E.; Tsitoni, K.; Moutsios, I.; Manesi, G.-M.; Nikitina, E. A.; Chalmpes, N.; Moschovas, D.; Gournis, D.; Ivanov, D. A.; Avgeropoulos, A. Structure/Properties relationship of anionically synthesized diblock copolymers ″grafted to″ chemically modified graphene. *Polymers (Basel)* **2021**, *13* (14), 2308.
(67) Che, M.; Tench, A. J. Characterization and reactivity of molecular oxygen species on oxide surfaces. In *Advances in Catalysis*; Eley, D. D., Pines, H., Weisz, P. B., Eds.; Academic Press, 1983; Vol. *32*, pp 1−148.
(68) Chao, C. Y. H.; Kwong, C. W.; Hui, K. S. Potential use of a combined ozone and zeolite system for gaseous toluene elimination. *J. Hazard. Mater.* **2007**, *143* (1), 118−127.
(69) Zhang, L.; Li, L.; Cao, Y.; Yao, X.; Ge, C.; Gao, F.; Deng, Y.; Tang, C.; Dong, L. Getting insight into the influence of SO_2 on TiO_2/CeO_2 for the selective catalytic reduction of NO by NH_3. *Appl. Catal., B* **2015**, *165*, 589−598.
(70) Liu, H.; Chen, Z.; Wang, H.; You, C. Active centers response to SO_2 and H_2O poisoning over Fe-W-Ni exchanged zeolite for high-temperature NH_3-SCR: Experimental and DFT studies. *Appl. Surf. Sci.* **2021**, *570*, 151105.

https://doi.org/10.1021/acsomega.2c00120
ACS Omega 2022, 7, 9818−9833